

Asphalt-related temperature correction of deflections measured in central FWD tests on a concrete-over-asphalt composite pavement

Rodrigo Díaz Flores, Valentin Donev, Mehdi Aminbaghai, Raphael Höller, Lukas Eberhardsteiner, Martin Buchta & Bernhard L.A. Pichler

To cite this article: Rodrigo Díaz Flores, Valentin Donev, Mehdi Aminbaghai, Raphael Höller, Lukas Eberhardsteiner, Martin Buchta & Bernhard L.A. Pichler (2024) Asphalt-related temperature correction of deflections measured in central FWD tests on a concrete-over-asphalt composite pavement, International Journal of Pavement Engineering, 25:1, 2301454, DOI: [10.1080/10298436.2023.2301454](https://doi.org/10.1080/10298436.2023.2301454)

To link to this article: <https://doi.org/10.1080/10298436.2023.2301454>



© 2024 The Author(s). Published by Informa UK Limited, trading as Taylor & Francis Group



Published online: 17 Feb 2024.



Submit your article to this journal [↗](#)



Article views: 688







View related articles [↗](#)



View Crossmark data [↗](#)

Asphalt-related temperature correction of deflections measured in central FWD tests on a concrete-over-asphalt composite pavement

Rodrigo Díaz Flores ^a, Valentin Donev ^b, Mehdi Aminbaghai^a, Raphael Höller^a, Lukas Eberhardsteiner ^b, Martin Buchta^c and Bernhard L.A. Pichler ^a

^aInstitute for Mechanics of Materials and Structures, TU Wien (Vienna University of Technology), Vienna, Austria; ^bInstitute for Transportation, TU Wien (Vienna University of Technology), Vienna, Austria; ^cNievelt Labor GmbH, Höbersdorf, Austria

ABSTRACT

This study focuses on the seasonal variations observed in five Falling Weight Deflectometer (FWD) tests conducted on a well-instrumented composite pavement. The main objective is to investigate the underlying mechanisms driving these seasonal variations and propose a method to facilitate the comparison of the different FWD tests. The stiffnesses of concrete, asphalt, and cement-stabilised layers are characterised individually. The stiffness of the subgrade is back-calculated using multi-layered simulations. These simulations also enable computation of deflections for different asphalt temperatures. The results allow for developing a method which converts measured deflections into corrected deflections referring to an asphalt reference temperature. Remaining seasonal variations of the corrected deflections refer to the subgrade. Corresponding k -values of the AREA4 method correlate well with seasonal variations of the stiffness of the subgrade. Finally, an alternative temperature-correction approach, requiring measured deflections only, is developed. Corrected deflections allow for quantifying seasonal stiffness variations of the subgrade.

ARTICLE HISTORY

Received 13 July 2023
Accepted 27 December 2023

KEYWORDS

Field-testing; multi-layered; non-destructive testing; seasonal variation; composite slabs; FWD

1. Introduction

The properties of the subgrade and of the various layers of a pavement structure are required for an accurate assessment of its structural condition. One of the most widely used deflection testing devices for quantification of layer stiffnesses is the Falling Weight Deflectometer (FWD). During FWD tests, geophones measure the deflections caused by a standardised falling weight that impacts onto the surface of the pavement. The evaluation of FWD tests performed on composite pavements is challenging, because measured deflections are influenced by both the temperature-dependent stiffness of asphalt and the seasonal variations of the stiffness of the subgrade. The aim of the present paper is to separate these two contributions. To this end, comprehensive structural field-testing and material laboratory characterisation methods are combined with multi-layered modelling of the composite pavement structure.

Concrete-over-asphalt structures have been idealised, for modelling purposes, as a thin composite plate with either a bonded or an unbonded interface between the two layers (Khazanovich *et al.* 2001). A modular ratio has been prescribed, defined as the ratio between the moduli of the asphalt and the concrete layers (Ioannides and Khazanovich 1994, Smith *et al.* 2017). The back-calculated moduli are significantly influenced by the choice of the modular ratio (Smith *et al.* 2017), and identification of a realistic ratio is difficult. Furthermore, if the thickness of the asphalt layer is so large that the

assumptions used in the theory of thin plates become unrealistic, less accurate results will be obtained (Khazanovich *et al.* 2001, Smith *et al.* 2017), especially when dealing with high temperatures that cause the stiffness of asphalt to decrease significantly. In such cases, the use of multi-layered models is warranted.

Multi-layered models are frequently used for back-calculation of the thickness and the stiffness of every layer to best fit the deflections measured during FWD testing. Such models assume an axisymmetric behaviour of the pavement structure. Despite recent challenges to this assumption (Díaz Flores *et al.* 2022, 2023a, 2023b), they still constitute the most accurate description of the problem. The theoretical origin of multi-layered models is Boussinesq's theory (Boussinesq 1885). It was first applied to pavement structures by Burmister (1945a, 1945b). The introduction of layer stiffness matrices was a significant step ahead in the continuous development of these methods (Thomson 1950, Haskell 1953, Kausel and Roësset 1981). Explicit solutions for general surface and dislocation loads acting on a transversely isotropic half-space are available since the late 1980s (Pan 1989a, 1989b). Much of the recent work refers to the development of modern computational methods to improve the accuracy of the back-calculation, e.g. by using artificial neural networks to obtain elastic (Sharma and Das 2008, Ghanizadeh *et al.* 2020, Wang *et al.* 2021) or viscoelastic properties (Varma and Emin Kutay 2016, Chatti *et al.* 2017), a combination of artificial

neural networks with genetic algorithms (Rakesh *et al.* 2006, Li and Wang 2019), a hybrid neural network structure (Han *et al.* 2022), as well as knowledge discovery and data mining (Gopalakrishnan *et al.* 2013) to obtain the mechanical properties of every layer. Remarkably, viscoelastic pavement properties have been obtained based on data from embedded instrumentation under moving wheel loads (Levenberg 2013), also accounting for the dynamic influence of load-time histories (Madsen and Levenberg 2018) through inertial forces (Roussel *et al.* 2019). Still, despite the remarkable achievements of multi-layered models, their use for back-calculation methods is computationally rather expensive (Chatti *et al.* 2017). Furthermore, much experience is necessary when it comes to the definition of search intervals and to the interpretation of results, as the nature of the mathematical problem is ill-posed (Romeo *et al.* 2023), i.e. that different sets of thicknesses and stiffnesses reproduce (virtually) the same deflections.

The importance of correcting FWD results for seasonal variations of temperature and moisture and, therefore, for changes of the stiffness of individual layers has been pointed out, e.g. by Bohn *et al.* (1972) and Khazanovich *et al.* (2001). Most corrections have been developed for flexible pavements, mostly attributing the seasonal variations to the varying asphalt properties (Levenberg and Shah 2008, Yusoff *et al.* 2011, Specht *et al.* 2017). Deflections have been adjusted to different temperatures, for instance by developing deflection curves from synthetic databases for temperatures in the asphalt, e.g. between 5°C and 30°C (Bohn *et al.* 1972), and then adjusting the deflection at each geophone through linear (Chen *et al.* 2000), quadratic (García and Castro 2011, Chou *et al.* 2017, Zheng *et al.* 2019), and logarithmic (Kim *et al.* 1995) relations between deflections and temperature. Back-calculated moduli have been corrected by making use of the time-temperature superposition principle for the asphalt layers (Park and Kim 1997, Le *et al.* 2023), e.g. through correction factors that are logarithmic functions of temperature (Park *et al.* 2001). In the case of rigid and concrete-over-asphalt composite pavements, commonly evaluated with the ‘dense-liquid model’ (Westergaard 1926, 1948, Ioannides 1990), correction approaches have been mostly focused on the influence of temperature gradients, because the corresponding curling of slabs influences (i) the stresses experienced by the slab and by the subgrade (Ioannides and Khazanovich 1998, Schmid *et al.* 2023, Sorgner *et al.* 2023), (ii) the load transfer efficiency of the joints (Shoukry *et al.* 2005, Vandenbossche 2007, Muslim *et al.* 2022), and (iii) the accuracy of the back-calculation (Khazanovich *et al.* 2001). Few recommendations have been given regarding the correction of seasonal variations of the properties of individual layers.

The objective of this study is to enhance the interpretation and comparability of FWD tests performed on different seasons. Two main innovations are introduced: (i) A multi-layered model is used to simulate the results of five FWD tests performed, in summer, winter, and transitional periods, on an innovatively-equipped concrete-over-asphalt composite pavement structure. The field-testing site is equipped with temperature sensors, acceleration sensors, and asphalt strain gauges (Donev *et al.* 2023). Herein, laboratory and in situ characterisation provides access to the constant,

temperature-dependent, and seasonally varying stiffnesses of concrete, asphalt, and a cement-stabilised granular material, respectively. Only two unknowns are left for back-calculation: the constant thickness and the seasonally varying stiffness of the subgrade. (ii) In order to separate the influence of the temperature-dependent stiffness of asphalt from that of the seasonally varying stiffness of the subgrade, an asphalt-related temperature-correction approach is developed for deflections measured during FWD testing. It allows for translating deflections measured at any temperature into deflections which refer to an asphalt reference temperature of 20°C. Thus, the corrected deflections are only influenced by the seasonal changes of the stiffness of the subgrade. This provides the motivation to use corrected deflections in order to compute k -values of the dense-liquid model by means of the AREA method. Finally, an alternative correction approach is developed, which requires measured deflections only.

The paper is structured as follows. Section 2 presents experimental data from non-destructive structural testing at the field testing site and from material testing of concrete and asphalt performed in the laboratory. Section 3 refers to simulations of the multi-layered pavement structure subjected to central FWD loading. At first, the model is used to back-calculate properties of the subgrade. Then, it is used for a sensitivity analysis regarding the temperature of asphalt. The results allow for the development of the asphalt-related temperature correction of measured deflections. k -values of the dense-liquid model are quantified from corrected deflections, and the correlation of these k -values with elastic moduli of the subgrade is demonstrated. Section 4 contains the alternative correction approach which requires measured deflections only. Finally, in Section 5, conclusions are drawn.

2. In situ and laboratory characterisation of the stiffness of a composite pavement and its layers

2.1. Field-testing site equipped with temperature sensors, strain gauges, and accelerometers

Field data were measured at an innovatively-equipped field-testing site on the motorway A10, south of Salzburg (Donev *et al.* 2023). The concrete-over-asphalt composite pavement structure consists of six layers. The top concrete layer (index = tc) has a thickness $h_{tc} = 5.0$ cm, see Figure 1. It rests on a bottom concrete layer (index = bc), $h_{bc} = 22.0$ cm, an asphalt layer (index = a), $h_a = 8.2$ cm, a cement-stabilised granular layer (index = cs), $h_{cs} = 17.6$ cm, an unbound granular layer (index = ub), $h_{ub} = 31.4$ cm, and the local subgrade (index = sb). One concrete slab of the emergency lane is equipped with temperature sensors, asphalt strain gauges, and accelerometers.

- Six Pt100 temperature sensors are positioned along a vertical axis, see the dark-blue triangles in Figure 1(b). This axis has an in-plane distance from the centre of the slab, which amounts to 1.40 m in driving direction and to 1.00 m in lateral direction, see Figure 2. The eccentric arrangement of temperature sensors was chosen to minimise the influence of sensors on the structural behaviour of the pavement

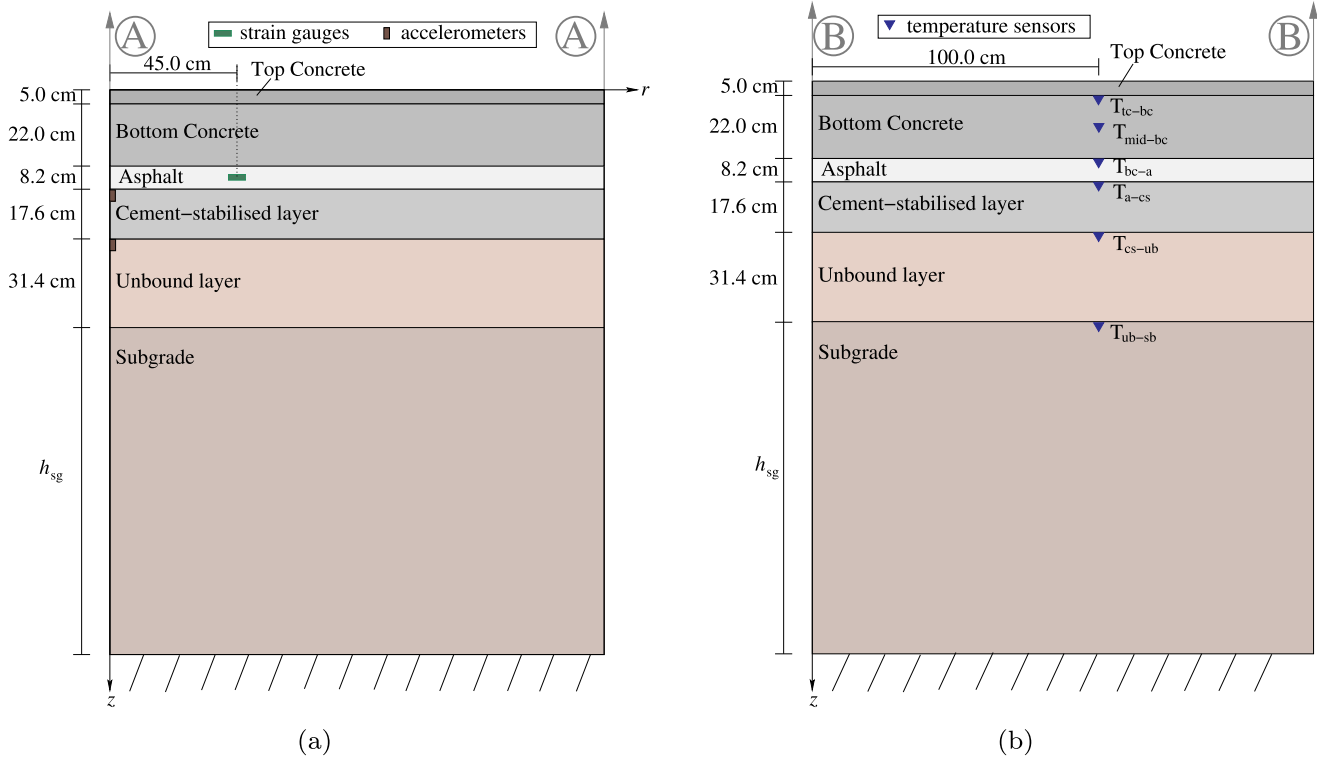


Figure 1. Cross-section of the investigated pavement structure and positions of (a) the accelerometers (dark-brown rectangles) and asphalt strain gauges (green lines), and (b) the temperature sensors (dark-blue triangles).

structure, as the loading was applied at the centre of the slab. Five Pt100 sensors are installed at the interfaces between neighbouring layers, while the sixth sensor is located at mid-depth of the bottom concrete layer, see Figure 1(b). This arrangement allowed for a detailed description of the temperature profile within the structure and for assessing whether temperature gradients within a layer were significant. The temperature at the surface of

the pavement was measured by means of a digital infrared thermometer.

- Four KM-100HAS strain gauges by Tokyo Measuring Instruments are installed at the bottom of the asphalt layer, at a depth of 33.0 cm underneath the surface and a radial distance of 45.0 cm from the centre of the slab, in a symmetric cross-wise arrangement, see the green lines in Figures 1(a) and 2. This arrangement of strain gauges allowed for the quantification of strains in radial direction. The distance from the centre of the slab was chosen based on Finite Element simulations, see Figure 7 of (Donev *et al.* 2023), considering a trade-off between obtaining reasonably large strain measurements, small strain gradients such that the measurements are easy to interpret, and large differences between measurements in the summer and winter seasons (Donev *et al.* 2023). One strain gauge was damaged during installation. Measurements from the remaining three sensors will be analysed in the present study.
- Two acceleration sensors are installed, one each at the top and at the bottom of the cement-stabilised granular layer, at depths of 35.2 cm and 50.8 cm, respectively, see the dark brown rectangles at the left boundary of Figure 1(a). This allowed for in situ characterisation of the elastic stiffness of the cement-stabilised layer through sledgehammer tests, see Section 2.5 and (Donev *et al.* 2023). The sensors were positioned at the centre of the slab, coinciding with the axis of loading, such that the arrival of longitudinal elastic waves can be accurately captured.

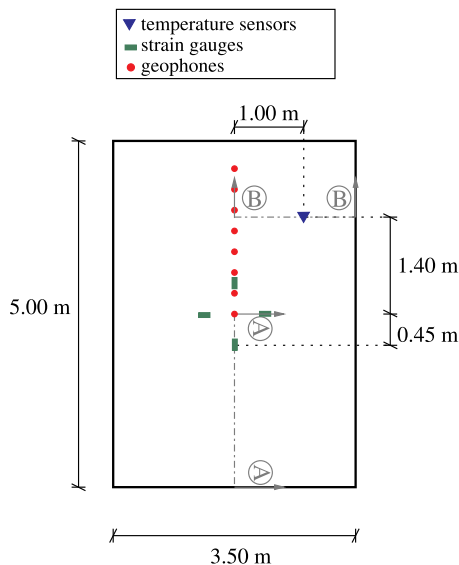


Figure 2. Top view of the investigated slab and positions of the temperature sensors (dark-blue triangles), the asphalt strain gauges (green lines), and the geophones (red dots).

The length and width of the instrumented slab amount to 5.00 m and 3.50 m, respectively, see Figure 2.

2.2. In situ stiffness characterisation of the composite pavement structure by means of FWD testing

FWD tests were performed at the field-testing site over five days from July 2021 until March 2022. The number and dates of FWD tests were chosen such that temperature profiles representative for summer (July and September), winter (January), and the transition periods (October and March) are obtained, see Table 1, also constrained by the availability of the used FWD equipment. On every test day, a minimum of 12 individual tests were performed. If time constraints allowed for it, even more tests were performed, resulting in up to 17 individual tests in October. This allowed for an accurate characterisation of pavement properties on different seasons during a full year.

All FWD tests were performed with a Dynatest 8082 trailer-mounted Heavy Weight Deflectometer, applying a maximum force of 200 kN. The number of FWD tests performed immediately one after the other, the average values of the maximum deflections measured by the eight geophones, and the average values of the maximum strains measured by the three functional asphalt strain gauges are listed in Table 2. Notably, FWD tests performed on the same testing date delivered very similar results, with low standard deviations and coefficients of variation, see Tables A1 and A2 in Appendix 1. No plastic deformation was observed as a consequence of the FWD tests, as no increasing nor decreasing trend was observed in the measured deflections. The measured deflections show a considerable seasonal variation, as shown by the results of the Analysis of Variance (ANOVA) presented in Table A3. The largest deflections were measured on the hottest FWD testing day in July 2021. They are by some 12% larger than the smallest deflections, which were recorded on the coldest field-testing day in January 2022. As regards days with similar temperature

Table 1. Temperatures measured at the field testing site on five FWD testing days: at the surface (T_{top-tc}), at mid-depth of the bottom concrete layer (T_{mid-bc}), and at the interfaces between neighbouring layers, e.g. T_{tc-bc} denotes the temperature at the interface between the top concrete (tc) and the bottom concrete (bc) layers, see also Figure 1(b).

Date	T_{top-tc} [°C]	T_{tc-bc} [°C]	T_{mid-bc} [°C]	T_{bc-a} [°C]	T_{a-cs} [°C]	T_{cs-ub} [°C]	T_{ub-sb} [°C]
Jul 21	25.5	24.7	22.4	22.1	22.4	21.1	19.6
Sep 21	20.5	19.2	17.3	17.6	18.2	18.9	18.3
Oct 21	10.5	10.5	8.8	9.0	9.6	11.0	12.7
Jan 22	-0.5	-0.6	-0.7	-0.3	0.1	0.7	1.5
Mar 22	8.5	8.7	8.5	9.2	9.7	9.8	8.4

tc = top concrete, bc = bottom concrete, a = asphalt, cs = cement-stabilised layer, ub = unbound layer, sb = subgrade

Table 2. Measurements from FWD experiments on the field-testing site, performed on five days: Average values (from n_{FWD} tests) of the maximum deflections measured by geophones at radial distances, r_i , measured from the centre of the slab, ranging from 0 to 2.1 m, and of the maximum strain obtained by the asphalt strain gauges (ϵ_{ASG}).

Date	n_{FWD}	Deflections [mm] measured at a radial distance of:								ϵ_{ASG} [10 ⁻⁶]
		$r_1 = 0.0$ m	$r_2 = 0.3$ m	$r_3 = 0.6$ m	$r_4 = 0.9$ m	$r_5 = 1.2$ m	$r_6 = 1.5$ m	$r_7 = 1.8$ m	$r_8 = 2.1$ m	
$t_1 =$ Jul 21	15	0.186	0.167	0.144	0.122	0.103	0.086	0.072	0.061	5.20
$t_2 =$ Sep 21	15	0.176	0.157	0.135	0.115	0.099	0.081	0.068	0.055	4.94
$t_3 =$ Oct 21	17	0.169	0.150	0.131	0.110	0.092	0.075	0.062	0.052	4.64
$t_4 =$ Jan 22	12	0.166	0.147	0.129	0.109	0.091	0.076	0.061	0.052	6.58
$t_5 =$ Mar 22	12	0.171	0.152	0.130	0.109	0.095	0.076	0.066	0.052	5.85

profiles, see October 2021 and March 2022, similar deflections (with difference of up to 3 μ m only) were measured. The measured strains range from 4.64×10^{-6} to 6.58×10^{-6} and show a less clear trend with temperature. The largest strain was measured in January 2022, when icy conditions prevailed in the depth of the asphalt layer. These conditions may have affected the experimental results, and may be the reason why the largest strain was measured during winter, and not during summer.

2.3. Laboratory stiffness characterisation of concrete by means of uniaxial compression tests

The stiffnesses of the top and bottom concrete layers were quantified in the laboratory. Three cylinders and three cubes of each of the two types of concrete were cast in situ from the same batches that were used to produce the slab. The cubic specimens had a side length of 0.15 m. The cylindrical specimens had a diameter of 0.07 m and a height of 0.34 m. The aspect ratio of the cylinders was chosen based on St. Venant's principle (Barré de Saint Venant 1855), as explained next. During testing, friction-induced shear stresses are activated at the interfaces between the load application system and the specimen (Karte *et al.* 2015, Irfan-ul Hassan *et al.* 2016). These undesired stresses decay with increasing distance from the interface. They become insignificant in an axial distance which is approximately equal to the diameter of the cylinders. The chosen dimensions ensured that the central region of the specimen, where deformations were measured, has an aspect ratio larger than 2:1. In addition, the diameter of 0.07 m was sufficiently larger than the size of the aggregates, in order to fulfil the separation of scales requirement (Zaoui 2002), i.e. to test representative volumes of concrete. After casting, the molds were sealed and the material was allowed to cure until testing at an age of 30 weeks.

The strength of both concretes was determined by crushing the cubes under uniaxial compression with a stress rate of 1 MPa/s. The cube compressive strength of the top and bottom concrete layer amounted to 65.4 MPa and 59.7 MPa, respectively, see Table 3.

The stiffness of each of the two concretes was determined by subjecting three cylindrical specimens to a series of nondestructive loading and unloading cycles, see also (Karte *et al.* 2015, Irfan-ul Hassan *et al.* 2016). Six cycles were performed for each specimen, three with a loading rate of 1 kN/s, and three with 20 kN/s. The maximum load was held constant for 10 s before the unloading began with the same rate as used for the loading. In order to avoid damage of the

Table 3. Cube compressive strength and unloading modulus of the top and bottom concrete.

Property	Top concrete	Bottom concrete
Cube compressive strength [MPa]	65.4	59.7
Unloading modulus [GPa]	34.1	46.3

specimens, the maximum load was limited to 15% of the cube compressive strength. The unloading modulus was quantified as the secant modulus of the unloading branch between 20% and 80% of the maximum load. The average of the 18 unloading moduli (six cycles and three specimens) amounted to 34.1 GPa for the concrete of the top layer and to 46.3 GPa for the concrete of the bottom layer, see Table 3. The corresponding standard deviations amounted to 0.27 GPa and 0.39 GPa, respectively.

All tests were performed at 20°C. The elastic modulus of cementitious materials remains virtually constant in the temperature range from 0 to 25°C (Vidal *et al.* 2015, Binder *et al.* 2023). During field-testing, the temperature of concrete ranged in this interval, see Table 1. Therefore, temperature-independent stiffness properties of concrete will be assumed throughout the rest of this study.

2.4. Laboratory stiffness characterisation of asphalt by means of cyclic uniaxial tension-compression tests

The viscoelastic properties of the asphalt were determined using direct tension-compression tests on cylindrical specimens according to Appendix 4 of the European Standard EN12697-26 (2018). Cylindrical specimens with height $h = 0.20$ m and diameter $d = 0.05$ m were manufactured in the laboratory using the asphalt sample that was collected during construction. At temperatures $T \in \{-10, -2.5, 2.5, 5, 10, 20, 30\}^\circ\text{C}$, the specimens were subjected to sinusoidal uniaxial tension-compression cycles imposed with frequencies $f \in \{0.1, 1, 3, 5, 8, 10\}$ Hz. The results of the tests were evaluated using a Dynamic Mechanical Analysis (DMA) (Planche *et al.* 1998, Chehab *et al.* 2002), the time-temperature superposition principle using the Williams-Landel-Ferry equation ($C_1 = 26.1$ and $C_2 = 181.3^\circ\text{C}$) (Williams *et al.* 1955), and the 2S2P1D model to approximate

a continuous function of the complex moduli, see Figure 3, Table 4, and Appendix 2.

16.7 Hz is the characteristic frequency of the dynamic load resulting from a falling weight in an FWD test. This frequency was chosen based on a review of many studies, see e.g. (Ullidtz and Stubstad 1985, Zhang *et al.* 2022, Fu *et al.* 2020, Tutumluer *et al.* 2009, Díaz Flores *et al.* 2023a, Roesset and Shao 1985), also taking into account that the first half-wave observed in the deflection histories measured in this study had a period of approximately 30 ms, see Figure 3 of (Díaz Flores *et al.* 2023a). The temperature-dependent dynamic modulus at 16.7 Hz is treated as an effective stiffness modulus of asphalt. It will be used as input for elastostatic analysis of FWD tests, see Figure 4(a).

Poisson's ratio of asphalt is also temperature- and frequency-dependent (Benedetto *et al.* 2007, Gudmarsson *et al.* 2015), rather than being constant (Aurangzeb *et al.* 2017, Lee and Kim 2009). In order to account for the influence of temperature, we use average values suggested in four studies (Graziani *et al.* 2014, Gudmarsson *et al.* 2014, Nguyen *et al.* 2021, Islam *et al.* 2015), see also Figure 4(b).

2.5. In situ stiffness characterisation of the cement-stabilised layer by means of accelerometer measurements recorded during sledgehammer tests

The stiffness of the cement-stabilised layer was quantified based on 'sledgehammer tests' performed at the centre of the instrumented slab (Donev *et al.* 2023). A rubber pad was put at the surface of the slab to ensure that it remained undamaged during the sledgehammer tests. A metal plate was put on top of the pad and hit by a sledgehammer to generate an elastic wave. The accelerometers described in Section 2 collected readings with a sampling rate of 200 kHz. Their signals are used to determine the time of arrival of the elastic wave both at the top and the bottom of the cement-stabilised layer. The time of arrival at each sensor is set equal to the time at which the first acceleration measurement is recorded outside the interval of white noise of the sensor. The difference of the two arrival times is equal to the time of flight of the wave through the layer, Δt . Dividing the thickness of the layer (17.6 cm) by the time of flight delivers the speed v_L of the elastic wave. Using the theory of propagation

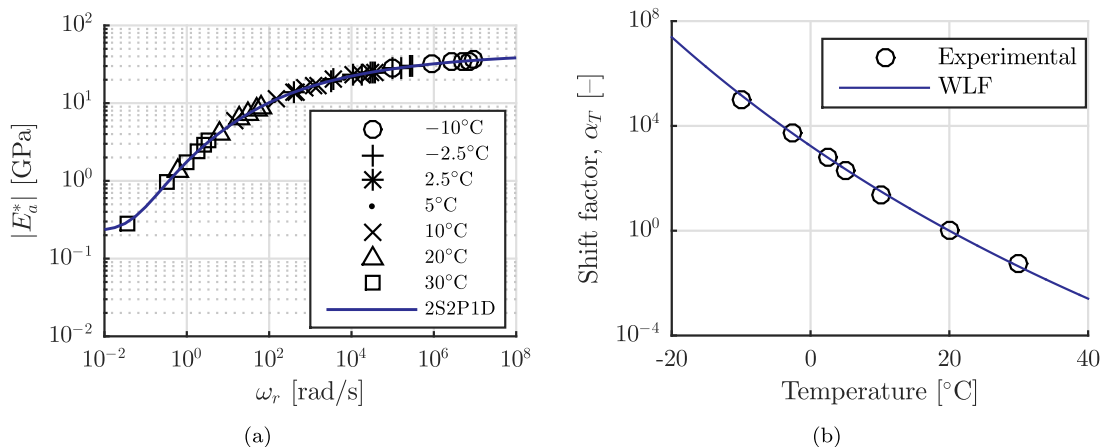
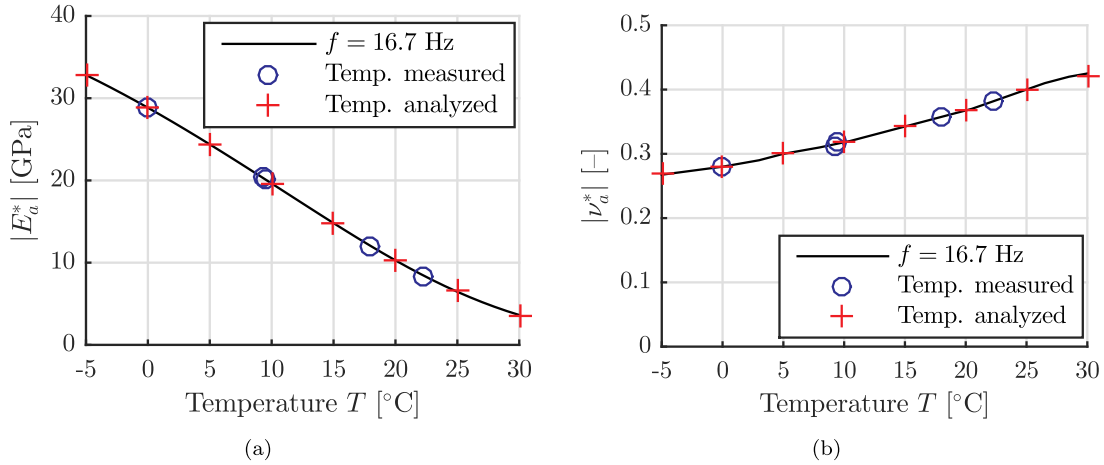


Figure 3. Viscoelastic properties of asphalt: (a) master curve for the dynamic modulus, $|E_a^*|$, as a function of the 'reduced' angular frequency $\omega_r = \alpha_T \omega$, and (b) horizontal shift factor, α_T , approximated by the Williams-Landel-Ferry Equation (A6).

Table 4. Parameters of the 2S2P1D model (Olard and Di Benedetto 2003, Di Benedetto *et al.* 2004) and the Williams–Landel–Ferry equation used in this study.

E_0 [MPa]	E_∞ [MPa]	δ [-]	h [-]	k [-]	τ_0 [s]	β [-]	C_1 [-]	C_2 [°C]
225.2	44480	1.843	0.5174	0.1837	0.004544	26.48	26.1	181.3

**Figure 4.** Temperature-dependent stiffness properties of asphalt at the FWD frequency of $f = 16.7$ Hz: (a) the dynamic modulus, as obtained from direct tension-compression tests, $|E_a^*|$, and (b) the norm of complex Poisson's ratio, which is set equal to the mean of the results suggested in (Nguyen *et al.* 2021, Graziani *et al.* 2014, Gudmarsson *et al.* 2014, and Islam *et al.* 2015), $|\nu_a^*|$; the solid line refers to the model, the circles to temperatures of asphalt measured during FWD testing, and the crosses to temperatures of asphalt considered during structural analysis.

of elastic bulk waves through isotropic media, see e.g. (Biot 1956, Bedford and Drumheller 1994), the elastic modulus of the cement-stabilised layer is quantified as

$$E_{cs} = \rho_{cs} v_L^2 \frac{(1 + \nu_{cs})(1 - 2\nu_{cs})}{1 - \nu_{cs}}, \quad (1)$$

where $\nu_{cs} = 0.20$ is the value of Poisson's ratio assigned to the cement-stabilised layer. Its mass density ρ_{cs} was determined in situ by excavating a hole, and by dividing the excavated mass (measured by means of a scale) by the volume of the hole. The volume was determined by laying a thin sheet of plastic into the hole, pouring water into it until the hole was filled, and then measuring the volume of water with a graduated cylinder. This process was performed three times, resulting in a mean mass density $\rho_{cs} = 2568$ kg/m³.

Since one sledgehammer test takes a few seconds only, several dozens of tests were performed every time shortly before an FWD test was carried out, see Table 5. The resulting database of times of flight, wave speeds, and stiffness moduli is evaluated statistically, see the mean values and standard deviations listed in Table 5. The elastic moduli determined from five sets of measurements, carried out between July 2021 and March 2022, range from 7.7 ± 1.6 GPa to 9.2 ± 1.2 GPa. These

Table 5. Results from n_{slh} sledgehammer tests performed on the instrumented slab: Δt denotes the time of flight through the cement-stabilised layer, v_L the speed of the wave passing through that layer, and E_{cs} its modulus of elasticity.

Date	n_{slh}	Δt [s]	v_L [m/s]	E_{cs} [GPa]
Jul 21	51	91.2 ± 7.3	1942 ± 150	8.74 ± 1.21
Sep 21	49	89.2 ± 7.3	1973 ± 161	9.16 ± 1.24
Oct 21	38	94.2 ± 3.9	1871 ± 77	8.05 ± 0.54
Jan 22	50	94.5 ± 4.7	1862 ± 93	8.08 ± 0.80
Mar 22	43	98.3 ± 9.7	1809 ± 186	7.70 ± 1.62

overlapping intervals underline a satisfactory degree of test repeatability and an only moderate seasonal dependence.

3. Multi-layered simulations and asphalt-related temperature correction of deflections

3.1. Multi-layered pavement structure subjected to FWD loading

Five datasets from FWD testing are analysed by means of radial-symmetric simulations, see Appendices 3, 4, and (Pan 1989a, 1989b). The pavement structure is represented as a body consisting of six layers with finite thickness and infinite in-plane dimensions, see Figure 1: top-concrete, bottom-concrete, asphalt, cement-stabilised layer, unbound layer, and subgrade. The boundary value problem regarding the static simulation of the multi-layered pavement structure subjected to the maximum FWD load is presented in Appendix 3.

The stiffness properties of the four topmost layers are known from laboratory and in situ tests. The elastic moduli of the top and bottom concrete amounted to 34.05 GPa and 46.25 GPa. Their Poisson's ratio amounted to 0.20. The stiffnesses of the asphalt layer and the cement-stabilised material were season-dependent, see Table 6. Notably, the stiffness properties of the asphalt layer are accounted for by means of

Table 6. Elastic stiffness properties of the different layers of the analysed pavement structure throughout the year; the moduli of elasticity of the unbound layer and the subgrade are unknown.

Date	asphalt		cement-stabilised layer	
	$ E_a^* $ [GPa]	$ \nu_a^* $ [-]	E_{cs} [GPa]	ν_{cs} [-]
$t_1 =$ Jul 21	8.40	0.38	10.20	0.20
$t_2 =$ Sep 21	12.10	0.36	9.20	0.20
$t_3 =$ Oct 21	20.30	0.31	10.40	0.20
$t_4 =$ Jan 22	28.90	0.28	8.10	0.20
$t_5 =$ Mar 22	20.10	0.32	7.66	0.20

effective temperature-dependent dynamic moduli that contain an elastic and a viscoelastic contribution for the frequency $f = 16.7$ Hz, see Figure 4. Alternatively, a time-dependent viscoelastic pavement model may be adopted, see e.g. (Levenberg 2013). The dynamic nature of the test may be accounted for using dynamic load-time histories (Madsen and Levenberg 2018), as well as inertial forces (Roussel *et al.* 2019) obtained from a double integration of the deflection histories measured, see e.g. (Díaz Flores *et al.* 2023a). The stiffness properties of the unbound granular layer and the subgrade are unknown. Both layers are assumed to have the same stiffness since they could not be clearly distinguished from each other during rehabilitation of the motorway. From now on, the sandwich of both layers is referred to as ‘the subgrade’. Poisson’s ratio is set equal to 0.35 which is a typical value used for unbound granular layers (Omine *et al.* 1999, Strasse-Schiene-Verkehr 2018a). The modulus of elasticity will be identified in the following subsection.

The thicknesses of the five topmost layers were measured during the installation of the pavement structure, see Figure 1. The thickness of the subgrade is unknown. It will be identified in the following subsection.

3.2. Back-calculation of subgrade properties from measured deflections and validation based on measured strains

The thickness and the modulus of elasticity of the subgrade are unknown. Seasonal variations of the modulus of elasticity are taken into account, because the stiffness of unbound granular materials is known to be function of the temperature and moisture (Salour and Erlingsson 2013, Bayat 2009). Thus, one specific value of the modulus of elasticity will be determined for every testing date. This results in five different sought stiffness values, denoted as $E_{sg}(t_1)$, $E_{sg}(t_2)$, $E_{sg}(t_3)$, $E_{sg}(t_4)$, and $E_{sg}(t_5)$. The thickness of the subgrade, in turn, must have been the same during all five testing dates, resulting in just one additional optimisation parameter, denoted as h_{sg} .

In order to achieve the best-possible agreement between measured and simulated surface deflections, the thickness of the subgrade and its modulus of elasticity are optimised in the context of structural simulations. The boundary value problem of Subsection 3.1 is solved following Pan (1989a, 1989b), see Appendix 4. The following search intervals are introduced for the thickness and the modulus of elasticity:

$$h_{sg} \in [60, 160] \text{ cm}, \quad (2)$$

$$E_{sg}(t_i) \in [70, 120] \text{ MPa} \quad i = 1, 2, 3, 4, 5. \quad (3)$$

The search intervals are chosen based on the results of a preliminary sensitivity analysis. Inspired by the optimisation method described in (Irfan-ul Hassan *et al.* 2016), all search intervals are subdivided into 11 equidistant grid points. Combining 11 different thickness values with 11 different stiffness values results in 121 pairs of parameters. For all 121 combinations, FWD testing on the multi-layered composite pavement structure is simulated. The results allow for minimising the root mean squared error between measured

and simulated deflections:

$$\begin{aligned} & RMSE(h_{sg}, E_{sg}(t_1), E_{sg}(t_2), E_{sg}(t_3), E_{sg}(t_4), E_{sg}(t_5)) \\ &= \sqrt{\frac{1}{5} \sum_{d=1}^5 \frac{1}{8} \sum_{g=1}^8 [w(t_d, r_g) - u_z(r_g, z=0; h_{sg}, E_{sg}(t_d), |E_a^*(t_d)|, |\nu_a^*(t_d)|, E_{cs}(t_d))]^2} \rightarrow \min, \end{aligned} \quad (4)$$

where $w(t_d, r_g)$ denotes the deflection measured at date t_d (with $d = 1, 2, \dots, 5$) in the radial distance r_g from the centre of the falling weight (with $g = 1, 2, \dots, 8$), see Table 2. $u_z(r_g, z=0; h_{sg}, E_{sg}(t_d), |E_a^*(t_d)|, |\nu_a^*(t_d)|, E_{cs}(t_d))$ denotes the deflection obtained by numerical simulation at the radial distance r_g from the centre of the falling weight, at the surface of the structure ($z=0$), computed with thickness value h_{sg} and stiffness value $E_{sg}(t_d)$, see the search intervals in Equations (2) and (3), as well as with the stiffness properties $|E_a^*(t_d)|$, $|\nu_a^*(t_d)|$, and $E_{cs}(t_d)$ listed in Table 6. Optimal values were found *inside* the search intervals of Equations (2) and (3). This clarified that the chosen limits were acceptable, and there was no need to expand the intervals. The grid-point-based optimisation method was useful given that only the thickness and the stiffness of the subgrade were optimised. Clearly, many other alternative optimisation methods could have been applied, including the use of Artificial Neural Networks and Genetic Algorithms, see e.g. (Pichler *et al.* 2003), which do not require subdivision of search intervals. The achievable minimum of $RMSE$ according to Equation (4) amounts to 2.2 μm . The corresponding optimal value of the thickness of the subgrade is equal to 100 cm. The optimal stiffness moduli range from 85 to 110 MPa. They show an only moderate seasonal variation. The deflections obtained with the optimised simulations agree very well with the measured deflections, see Figure 5.

In order to validate the five back-calculation results, radial normal strains of asphalt, computed at the depth of 33 cm from the top surface of the pavement and the radial distance of 45 cm from the axis of symmetry, are compared with measured strains, see Table 8. Notably, the simulated asphalt strains agree well with the measured maxima of the strain sensor readings. The prediction error amounts, on average, to 8.4%. This is acceptable for an application in geotechnical engineering and, thus, corroborates the results of the back-calculation activity.

3.3. Development of an asphalt-related temperature correction for measured surface deflections

Performing nominally *identical* FWD tests at *the same* spot on *the same* composite pavement structure, but at different dates and, therefore, at *different* temperatures, yields *different* surface deflections measured by the geophones, see Table 2. It is desirable to correct the measured deflections such as to obtain deflections that would have been measured provided that the temperature in the asphalt layer had amounted to the reference temperature $T_{ref} = 20^\circ\text{C}$. Corrected deflections from different dates will still be different. These differences will refer to seasonal stiffness changes of the subgrade.

For the described asphalt-related temperature correction of deflections measured during FWD testing, the following ansatz

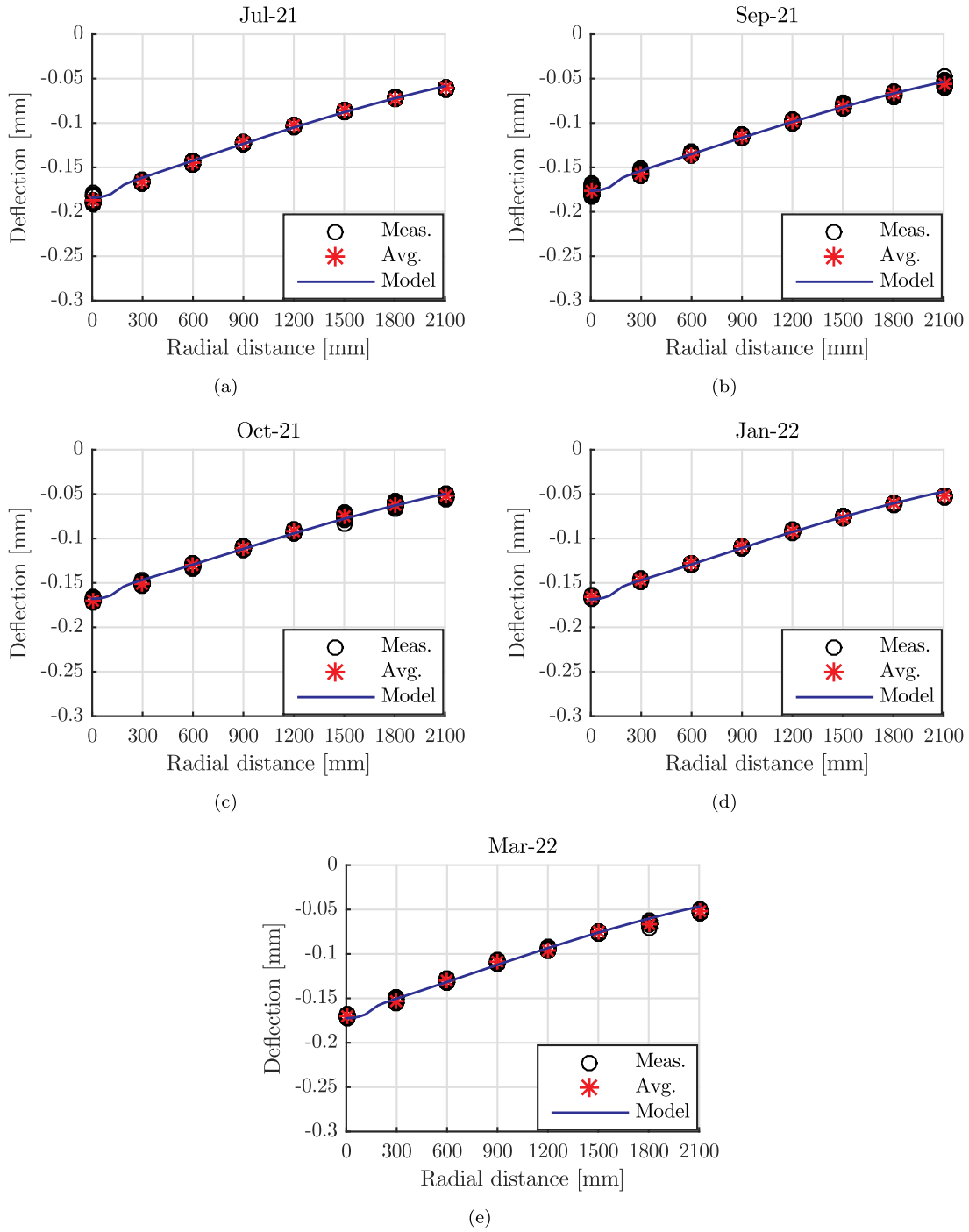


Figure 5. Results of multi-layered analysis: the blue solid lines illustrate surface deflections obtained with optimised values of the stiffness and the thickness of the subgrade, see Table 7, and comparison with measured deflections, see the circles (= individual measurements) and stars (= mean values); for different testing dates: (a) Jul 21, (b) Sep 21, (c) Oct 21, (d) Jan 22, and (e) Mar 22.

is made:

$$w^{corr}(r) = w(r, T_a) - w_{ref} \times \gamma(r, T_a), \quad (5)$$

where $w(r, T_a)$ stands for deflections measured at radial distance r , and the functional argument T_a refers to the temperature of the asphalt layer at the time of FWD testing. In addition, w_{ref} denotes a reference deflection, $\gamma(r, T_a)$ a dimensionless correction function, and $w^{corr}(r)$ the corrected deflections. Westergaard’s solutions for an infinite plate on top of a Winkler foundation (Westergaard 1926, 1948) are the source of inspiration for the following choice of the correction

function $\gamma(r, T_a)$:

$$\gamma(r, T_a) = \begin{cases} b_1 \left(1 - 10^{b_2 \frac{T_a - T_{ref}}{T_{ref}}} \right) \dots \dots \dots r \leq R, \\ k_1 \left(1 - 10^{k_2 \frac{T_a - T_{ref}}{T_{ref}}} \right) \ker\left(\frac{r}{r_0}\right) + k_3 \left(1 - 10^{k_4 \frac{T_a - T_{ref}}{T_{ref}}} \right) \text{kei}\left(\frac{r}{r_0}\right) \dots r > R, \end{cases} \quad (6)$$

where \ker and kei are Kelvin Bessel functions.

Table 7. Back-calculated values of the thickness h_{sg} and of the modulus of elasticity E_{sg} of the subgrade, as well as comparison with the temperatures measured at the interface between unbound granular layer and the subgrade, T_{ub-sb} .

Date	h_{sg} [cm]	E_{sg} [GPa]	T_{ub-sb} [°C]
$t_1 = \text{Jul 21}$	100	0.085	19.6
$t_2 = \text{Sep 21}$	100	0.095	18.3
$t_3 = \text{Oct 21}$	100	0.100	12.7
$t_4 = \text{Jan 22}$	100	0.110	1.5
$t_5 = \text{Mar 22}$	100	0.105	8.4

Table 8. Validation of back-calculation results: comparison of measured asphalt strains, ε_{ASG} with simulated strains, ε_{sim} , and comparison with the temperature measured at the top and bottom of the asphalt layer, T_{top-a} and T_{bot-a} , as well as with the stiffnesses of the asphalt and the cement-stabilised layers, $|E_a^*|$ and E_{cs} .

Date	ε_{ASG} [10 ⁻⁶]	ε_{sim} [10 ⁻⁶]	T_{top-a} [°C]	T_{bot-a} [°C]	$ E_a^* $ [GPa]	E_{cs} [GPa]
$t_1 = \text{Jul 21}$	5.20	5.75	22.1	22.4	8.4	10.20
$t_2 = \text{Sep 21}$	4.94	5.15	17.6	18.2	12.1	9.20
$t_3 = \text{Oct 21}$	4.64	5.03	9.0	9.6	20.3	10.40
$t_4 = \text{Jan 22}$	6.58	5.39	-0.3	0.1	28.9	8.10
$t_5 = \text{Mar 22}$	5.85	5.76	9.2	9.7	20.1	7.66

In order to identify the constants b_1 , b_2 , k_1 , k_2 , k_3 , and k_4 eight simulations of the multi-layered pavement structure are performed according to Subsection 3.1 and Appendix 4. Thereby, the temperature of the asphalt is set equal to the eight values ranging from -5°C to $+30^\circ\text{C}$. Corresponding stiffness values are listed in Table 9, see also the red crosses in Figure 4.

The stiffness values of all other layers are set constant. The ones assigned to the concrete layers are taken from Table 6. The moduli of elasticity of the cement-stabilised and subgrade layers are set equal to $E_{cs} = 8.35$ GPa and $E_{ub} = E_{sg} = 0.10$ GPa, respectively. These are the mean values computed on the basis of five values listed in Table 5 and in Table 7, respectively. In addition, the following values of Poisson's ratio are assigned to the cement-stabilised and subgrade layers: $\nu_{cs} = 0.20$ and $\nu_{ub} = \nu_{sg} = 0.35$, see Table 6. The eight computed deflection curves portray the influence of the temperature-dependent stiffness of asphalt on the FWD-response of the composite pavement structure, see Figure 6.

The eight computed deflection curves are inserted as $w(r, T_a)$ into the right-hand-side of Equation (5) and the unknowns in the definition of $\gamma(r, T_a)$ are identified such that Equation (5) delivers corrected deflection curves which come as close as possible to the simulated deflection curve referring to $T_a = T_{ref} = 20^\circ\text{C}$. Thereby, w_{ref} is set equal to the simulated deflection at the axis of symmetry ($r=0$), obtained with $T_a = 20^\circ\text{C}$, i.e. $w_{ref} = 179 \mu\text{m}$, and r_0 is set equal to 2.1 m, see Table 10 also for the identified values of b_1 , b_2 , k_1 , k_2 , k_3 , and k_4 .

In order to demonstrate the performance of the developed correction, it is applied to the simulated deflections shown in Figure 6. The corrected deflections indeed form a master curve, see Figure 7.

Table 9. Variation of the temperature of the asphalt layer, T_a , and corresponding values of the dynamic stiffness properties, $|E_a^*|$ and $|\nu_a^*|$, at the FWD frequency $f = 16.7$ Hz, see also Figure 4.

T_a [°C]	$ E_a^* $ [GPa]	$ \nu_a^* $ [-]
-5	32.8	0.27
± 0	28.8	0.28
5	24.4	0.30
10	19.6	0.32
15	14.8	0.34
20	10.3	0.37
25	6.5	0.40
30	3.6	0.42

3.4. Application of the asphalt-related temperature correction to deflections measured during FWD testing

The deflections measured during the five FWD tests, see Table 2 and Figure 8(a), are subjected to the asphalt-related temperature correction of Equations (5) and (6), see also Table 10. Thereby, the temperature of asphalt is set equal to the mean of the values measured at the top and the bottom of the asphalt layer: $T_a = (T_{top-a} + T_{bot-a})/2$, see Table 8. The corrected deflections are illustrated in Figure 8(b), see also Table A4.

The seasonal differences of the measured deflections decrease with increasing distance from the centre of the falling weight, see Figure 8(a). The seasonal differences of the corrected deflections, in turn, are similarly large independent of the distance from the centre of the falling weight, see Figure 8(b). These remaining differences result mainly from seasonal changes of the stiffness of the subgrade. This will be demonstrated in the following two subsections.

3.5. Evaluation of corrected deflections: quantification of k-values by means of the dense-liquid model and the AREA-method

Corrected deflections are evaluated by means of the AREA-method, initially introduced for flexible pavements by Hoffman and Thompson (1980). It idealises a pavement structure as a plate resting on a Winkler foundation exhibiting a uniform spring stiffness per unit area, k_{sg} , often referred to as 'modulus of subgrade reaction' and herein referred to simply as 'k-value', see Figure 9.

The AREA parameter is equal to the normalised area under the deflection curve $w(r)$, see e.g. (Hoffman and Thompson 1980). Herein, $w(r)$ is integrated from the axis of the falling weight to the position of the fourth geophone, and the integral is numerically approximated using the trapezoidal rule. This yields the AREA4 parameter (Khazanovich *et al.* 2001) as:

$$\begin{aligned} \text{AREA4} &= \frac{1}{w_1} \int_0^{3\Delta r} w(r) dr \\ &\approx \frac{1}{2} \left[\Delta r + 2\Delta r \left(\frac{w_2}{w_1} \right) + 2\Delta r \left(\frac{w_3}{w_1} \right) + \Delta r \left(\frac{w_4}{w_1} \right) \right], \end{aligned} \quad (7)$$

where w_i (with $i = 1, 2, 3, 4$) refers to surface deflections at a

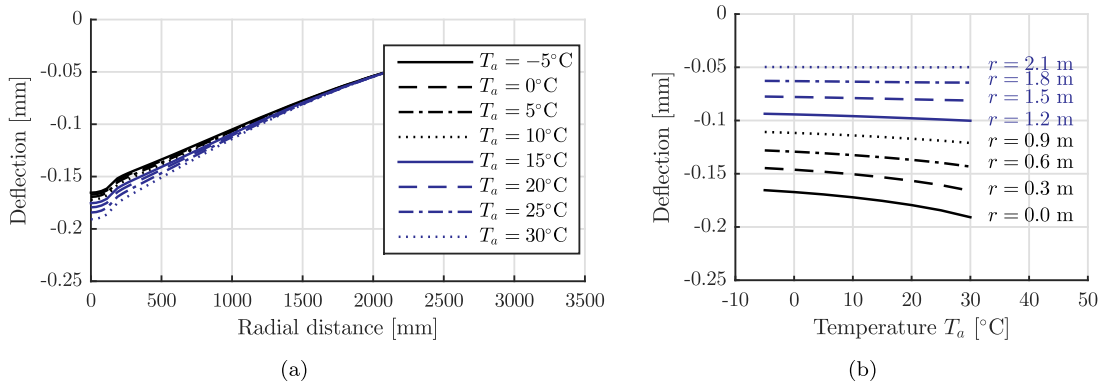


Figure 6. Deflections of the surface of the composite pavement structure as a function of (a) the radial distance from the axis of symmetry, for different temperatures of the asphalt layer, and (b) the temperature of the asphalt layer, for different radial distances from the axis of symmetry.

Table 10. Values of constants which are part of the mathematical expressions describing the asphalt-related temperature correction of deflections measured during FWD testing, see Equations (5) and (6).

$b_1 = -0.1065$	$b_2 = 0.4456$	$T_{ref} = 20^\circ\text{C}$	$w_{ref} = 179 \mu\text{m}$	$r_0 = 2.1 \text{ m}$
$k_1 = -0.0442$	$k_2 = 0.5250$	$k_3 = -0.0104$	$k_4 = 0.8903$	

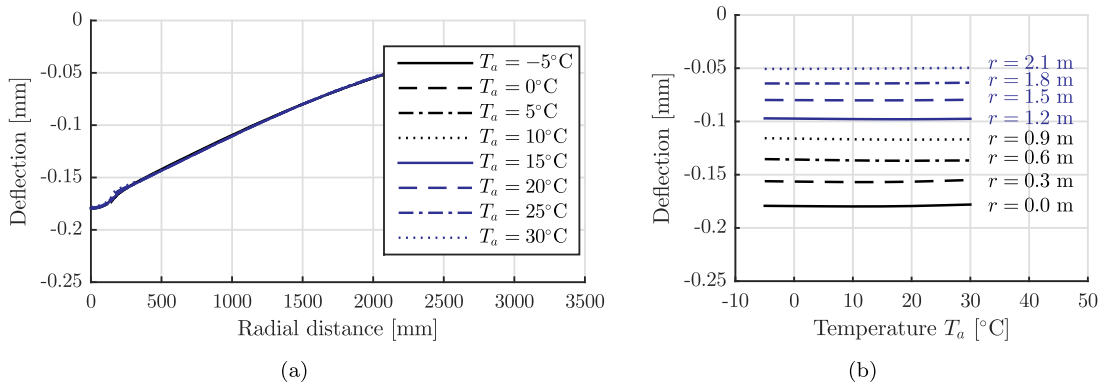


Figure 7. Results obtained from application of the correction Equations (5) and (6), see also Table 10, to the deflection curves illustrated in Figure 6.

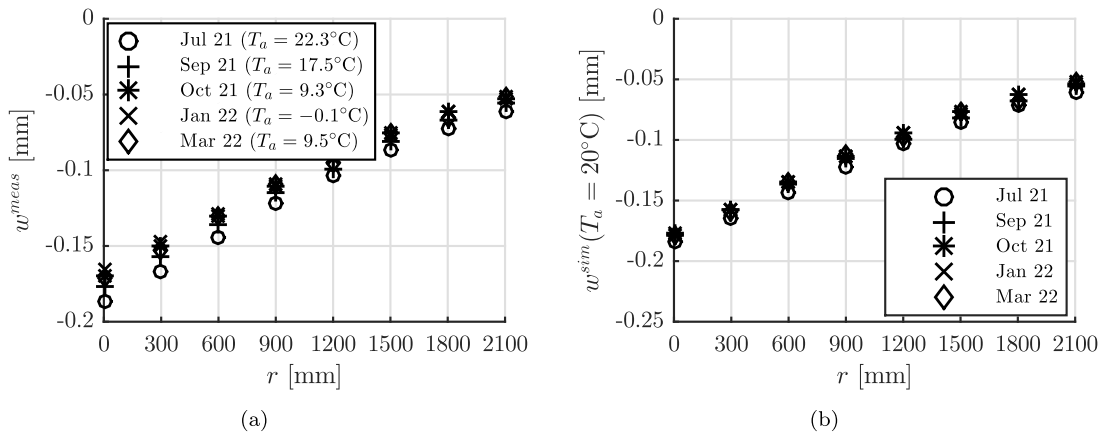


Figure 8. (a) Surface deflections measured during FWD testing at the field-testing site: the illustrated values are taken from Table 2, and (b) results obtained from subjecting the measured deflections of Table 2 to the asphalt-related temperature correction of Equations (5) and (6), see also Table 10.

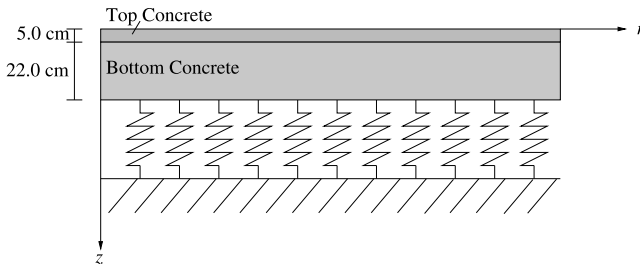


Figure 9. Dense-liquid model: elastic plate on a Winkler foundation.

radial distance of $r = (i - 1) \Delta r$, with $\Delta r = 300$ mm. The relationship between the AREA4 parameter and the radius of relative stiffness l_k was derived in the context of a non-dimensional approach (Losberg 1960, Ioannides 1990, Ioannides *et al.* 1989), using Westergaard's solutions for the 'dense-liquid' model (Westergaard 1926, 1948):

$$l_k = \left(\frac{D}{k_{sg}} \right)^{0.25} = \left[\frac{\ln \left(\frac{\xi_1 - \text{AREA4}}{\xi_2} \right)}{\xi_3} \right]^{\xi_4} \times 1 \text{ mm}, \quad (8)$$

where D is the bending stiffness of the plate. For the here-used configuration of four equidistant geophones with $\Delta r = 300$ mm, the ξ -parameters in Equation (8) take the values listed in Table 11, see also (Hall *et al.* 1997) for other sensor configurations. The numerical value of D is set equal to the bending stiffness of the sandwich plate made from the two topmost concrete layers, see Appendix 5 for the derivation of $D = 71.11 \text{ MPa m}^3$.

The k -values are quantified as follows. Corrected deflections referring to the five different FWD testing dates are inserted, one after the other, into Equation (7), the resulting values of AREA4 are inserted together with $D = 71.11 \text{ MPa m}^3$ and the ξ -parameters according to Table 11 into Equation (8), and the resulting expression is solved for k_{sg} . This yields k -values listed in Table 12.

3.6. Correlation of stiffness properties quantified by means of multi-layered and dense-liquid models

FWD tests are *non-destructive* experiments and both the multi-layered model as well as the dense-liquid model are *linear* simulation approaches. Therefore, there must be a directly-proportional relation between seasonally changing stiffness properties of both simulation approaches. This will be studied next.

The k -values quantified from *corrected* deflections, see Table 12, are correlated with corresponding elastic moduli of the subgrade, see Table 7. The correlation coefficient, r , amounts to 0.96, see Figure 10. This implies that k -values quantified from corrected deflections correlate very well with the elastic modulus of the subgrade. This can be explained as follows. The developed method for correction of measured deflections removes the part of the deflections that varies because of the

Table 11. Values of the ξ -parameters in Equation (8).

$\xi_1 = 914.4 \text{ mm}$	$\xi_2 = 46031.89 \text{ mm}$	$\xi_3 = -1.224177$	$\xi_4 = 4.387009$
----------------------------	-------------------------------	---------------------	--------------------

Table 12. k -values calculated from the corrected deflections, see Table A4 and Figure 8(b).

Date	k_{sg} [MPa/m]
Jul 21	163.59
Sep 21	187.28
Oct 21	197.35
Jan 22	206.65
Mar 22	210.09

influence of the asphalt layer. The remaining variations of the corrected deflections mainly refer to the subgrade.

3.7. Robustness of results with respect to the uncertainty regarding D

The k -values were computed based on the value of $D = 71.11 \text{ MPa m}^3$. In the following, it is explained that the correlation coefficient given in Figure 10 stays the same, even if a different value of D is used for quantification of the k -values. Provided that the value of $D = 71.11 \text{ MPa m}^3$ is scaled by a factor p , corresponding values of k_{sg} are scaled by the same factor p , because the ratio D/k_{sg} must stay the same according to Equation (8), i.e. $l_k = D/k_{sg} = (pD)/(pk_{sg})$. Multiplying all k -values in Figure 10 by the same arbitrary scaling factor p yields *the same* correlation coefficient. Thus, the essential result of the present study is perfectly robust with respect to the uncertainty regarding the bending stiffness of the plate of the dense-liquid model.

4. Alternative correction approach requiring measured deflections only

The correction approach developed in Section 3 requires reliable multi-layered simulations and knowledge of the temperature of the asphalt layer during FWD testing. Both ingredients were available in Section 3 because FWD testing was performed on a well-instrumented filed testing site. In standard FWD testing, however, knowledge regarding the thicknesses, stiffnesses, and temperatures of the layers of the hit pavement structure is frequently very limited. The temperature of the asphalt layer can be determined e.g. by drilling a small hole from the top of the pavement down to the asphalt layer, see e.g. (Strasse-Schiene-Verkehr

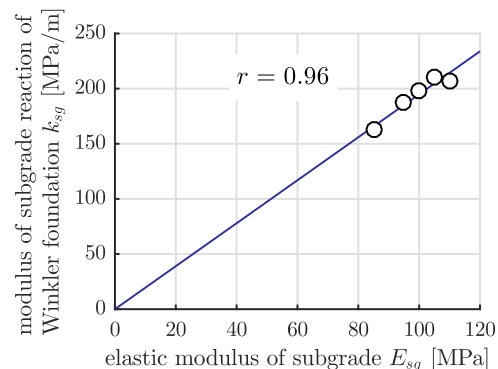


Figure 10. Correlation between k -values quantified from *corrected* displacements and elastic moduli of the subgrade.

2018b), but this still does not provide enough knowledge for the calibration of the correction approach presented in Section 3. As a remedy, an alternative correction approach is developed. It requires knowledge of measured deflections only. Its development exploits the following findings regarding the influence of asphalt and subgrade stiffnesses on surface deflections.

4.1. Influence of asphalt and subgrade stiffnesses on surface deflections

The influence of the stiffness of asphalt on surface deflections decreases with increasing distance from the axis of the falling weight, see Figure 6. This implies that stiffness changes of asphalt result, during FWD tests performed at different dates, in *different curvatures* of the surface of the concrete slab.

The influence of the stiffness of the subgrade on surface deflections, in turn, is virtually constant in the region of the geophones, see Figure 8(b). This implies that stiffness changes of the subgrade result, during FWD tests performed at different dates, in almost *the same curvature* of the surface of the concrete slab, but in different absolute values of the deflections. This is the motivation for the following engineering correction of measured surface deflections.

4.2. Engineering correction, based on measured deflections only

As for seasonally-repeated FWD testing on regular (= non-instrumented) composite pavements, a correction approach which requires only measured deflections is developed. The first FWD results serve as the reference: $t_1 = t_{ref}$. All subsequent FWD results are corrected such that they refer to the asphalt temperature at time $t_1 = t_{ref}$, even if this temperature is unknown. To this end, the deflections measured at $t_1 = t_{ref}$ are uniformly shifted:

$$w_{eng}^{corr}(r, t_d) = w(r, t_{ref}) + \Delta w(t_d). \quad (9)$$

The amount by which the deflections are shifted is chosen such that the corrected deflections are equal to measured deflections

at the radial distance $r_6 = 1500$ mm, see also Figure 11:

$$\Delta w(t_d) = w(r_6, t_d) - w(r_6, t_{ref}). \quad (10)$$

Applying Equations (9) and (10) to the measured deflections, see Figure 8(a) and Table 2, yields alternatively corrected deflections illustrated in Figure 12, see also Table A5. The corrected deflections refer to exactly *the same curvature* of the surface of the concrete slab, but to different absolute values.

The radial position r_6 , which plays a prominent role in the corrections approach of Equations (9) and (10), is the result of the following trade-off considerations. The radial position showing up in Equation (10) shall be (i) suitably far away from the axis of the falling weight, such that deflections measured at this distance are not significantly influenced by temperature-dependent stiffness changes of asphalt, and (ii) suitably close to the axis of the falling weight, such that deflections measured at this distance still show significant variations resulting from seasonal stiffness changes of the subgrade.

4.3. Application of the AREA4-approach for quantification of k-values from alternatively corrected deflections

In the following, it will be shown that the alternative correction approach yields deflections which are similarly expressive as the ones obtained from the application of the corrections approach of Section 3. To this end, k -values will be computed

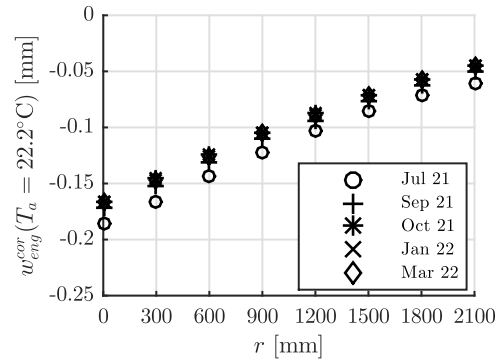


Figure 12. Alternatively corrected deflections: results obtained from subjecting the measured deflections of Table 2 to the correction of Equations (9) and (10).

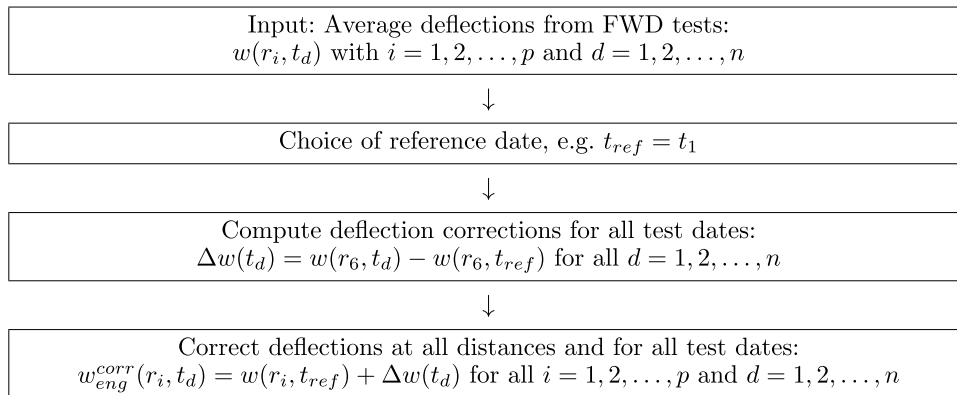


Figure 11. Flow chart for the use of the alternative correction method.

from the newly corrected deflections, and the season-dependent k -values will be correlated with season-dependent values of the stiffness of the subgrade.

The AREA4-values of the deflections corrected according to Equations (9) and (10) can be expressed as:

$$AREA4_{eng}^{corr}(t_d) = \frac{AREA4(t_{ref}) \times w_1(t_{ref}) + 3\Delta r \times \Delta w(t_d, t_{ref})}{w_1(t_{ref}) + \Delta w(t_d, t_{ref})}, \quad (11)$$

where $AREA4(t_{ref}) \times w_1(t_{ref})$ denotes the area under the reference deflection curve in the interval from $r = 0$ to $r = 3\Delta r$, the expression $3\Delta r \times \Delta w(t_d, t_{ref})$ is equal to the change of that area resulting from shifting, and $w_1(t_{ref}) + \Delta w(t_d, t_{ref})$ is equal to the value of the shifted deflections at the axis of the falling weight.

Corresponding k -values are quantified by inserting the AREA4-values according to Equation (11), together with $D = 71.11 \text{ MPa m}^3$ and the ξ -parameters according to Table 11, into Equation (8), and by solving the resulting expression for k_{sg} . This yields the k -values listed in Table 13.

In order to assess the quality of the correction according to Equations (9) and (10), the corresponding k -values from Table 13 are correlated with k -values from deflections corrected according to Equations (5) and (6), see Table 12, and with the elastic moduli of the subgrade listed in Table 7. The results of this comparison, see Figure 13, underline that the engineering correction of Equations (9) and (10), which requires knowledge of measured deflections only, allows for similar conclusions regarding the stiffness of the subgrade as the more advanced correction of Equations (5) and (6), which requires knowledge of the temperature of asphalt and realistic

multi-layered simulation of the investigated pavement structure.

5. Conclusions

From the results of the presented study, the following conclusions are drawn:

- The seasonal variations of deflections measured during the analysed FWD tests mainly result from (i) the strong temperature-dependence of the stiffness of the relatively thin layer of asphalt, and (ii) the milder season-dependence of the stiffness of the relatively thick layer of the subgrade.
- The variations of *corrected* deflections mainly result from the season-dependent stiffness of the subgrade, as clarified by the very good correlation between the k -values of a dense-liquid model, derived from deflections corrected according to Equations (5), (6), and Table 10, and the seasonal variations of the elastic modulus of the subgrade, see Figure 10.
- The alternative correction approach delivers useful estimates of relative seasonal stiffness changes of the subgrade, as clarified by the good correlation between k -values, derived from deflections corrected according to Equations (9) and (10), and the seasonal variations of the elastic modulus of the subgrade, see Figure 13.
- The temperature-correction of measured deflections is appealing because corrected deflections allow for the application of any method typically used for interpretation of FWD results, including deflection basin parameters and structural models.

Finally, the limitations of the present study are addressed.

- The proposed correction methods were applied to FWD test data from one specific concrete-over-asphalt composite pavement structure. In the future, it will be interesting to apply the here-developed engineering correction approach also to FWD data from repeated testing of other composite pavements.

Table 13. k -values calculated from the deflections corrected according to Equations (9) and (10), see also Figure 12 and Table A5.

Date	k_{sg}^{eng} [MPa/m]
Jul 21	168.91
Sep 21	197.54
Oct 21	218.69
Jan 22	215.82
Mar 22	217.72

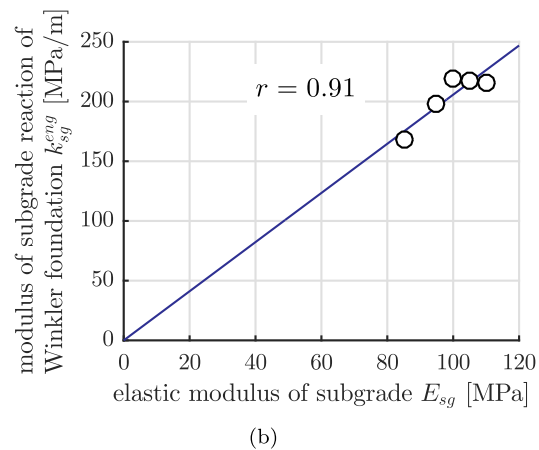
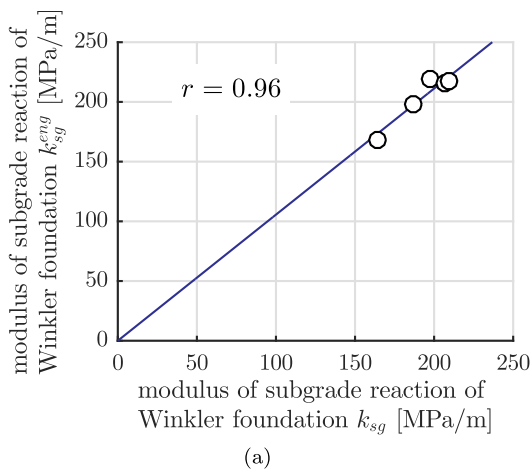


Figure 13. Correlation between k_{cor}^{eng} -values from Table 13, referring to the engineering correction approach of Equations (9) and (10), with (a) k -values from the first presented correction approach of Equations (5) and (6), see Table 12, and (b) the elastic modulus of the subgrade, E_{sg} , from Table 7. The correlation is quantified using the correlation coefficient r .

- The investigated pavement was young and undamaged. In the future, it will be interesting to verify the applicability of the correction methods to more aged, potentially damaged pavements, as well as temperatures larger than 35°C.
- A static, quasi-elastic simulation of the FWD test was performed, assuming effective stiffness properties containing elastic and viscoelastic contributions of the asphalt layer. In the future, it will be interesting to perform a viscoelastic simulation under the additional consideration of inertia forces.
- The geological situation is quite variable along the motorway A10. In other words, it is likely that the subgrade properties (mineralogy, thickness, etc.) are virtually constant along short stretches of the motorway only. Therefore, in the interest of comparability, future FWD tests should be carried out on the same slab. In cases where the geological situation is quite stable, in turn, testing on different slabs of a motorway section and comparing the obtained results appears to be reasonable.
- The asphalt strain gauges were positioned such that they measure radial strains, as redundant measurements were desired and it was only possible to install four sensors. In the future, it will be interesting to also measure strains in the tangential direction, such that the structural model used can be further validated.

Acknowledgments

Interesting discussions with Christian Hellmich and Luis Zelaya-Lainez are gratefully acknowledged. Help of Olaf Lahayne, Wolfgang Dörner, Dominic Hassan, Michael Haminger, and Constantin Kreil, as well as David Valentin and Bernhard Hadler (TU Wien) concerning laboratory testing is also gratefully acknowledged. Michael Celadnik and Harald Aigner (Nievelt Labor GmbH, Austria) are also acknowledged for conducting FWD measurements and interesting discussions. The authors acknowledge TU Wien Bibliothek for financial support through its Open Access Funding Programme.

Disclosure statement

No potential conflict of interest was reported by the author(s).

Funding

This research received financial support by the Austrian Research Promotion Agency (FFG) within the Bridge Project 2021 ‘Grundlegende Analyse von FWD-Versuchen: innovative Experimente, moderne Struktursimulationen, statistische Datenanalyse – FALLINGweight’. The authors also acknowledge the TU Wien University Library for financial support through its Open Access Funding Programme.

ORCID

Rodrigo Díaz Flores  <http://orcid.org/0000-0002-1153-9875>
 Valentin Donev  <http://orcid.org/0000-0002-3933-971X>
 Lukas Eberhardsteiner  <http://orcid.org/0000-0003-2153-9315>
 Bernhard L.A. Pichler  <http://orcid.org/0000-0002-6468-1840>

References

Aurangzeb, Q., et al., 2017. Viscoelastic and Poisson's ratio characterization of asphalt materials: critical review and numerical simulations. *Materials and Structures*, 50 (1), 1–12.

- Barré de Saint Venant, A.J.C., 1855. Mémoire sur la torsion des prismes, [memory on twisting prisms], mémoires des savants étrangers [memoires of foreign scholars]. *Comptes Rendues de l'Académie des Sciences*, 14, 233–560.
- Bayat, A., 2009. *Field and numerical investigation to determine the impact of environmental and wheel loads on flexible pavement*. Thesis (PhD). University of Waterloo.
- Bedford, A., and Drumheller, D., 1994. *Elastic wave propagation*. John Wiley & Sons, 151–165.
- Benedetto, H.D., et al., 2007. Three-dimensional linear behavior of bituminous materials: experiments and modeling. *International Journal of Geomechanics*, 7 (2), 149–157.
- Binder, E., et al., 2023. Thermally activated viscoelasticity of cement paste: minute-long creep tests and micromechanical link to molecular properties. *Cement and Concrete Research*, 163, 107014.
- Biot, M.A., 1956. Theory of propagation of elastic waves in a fluid-saturated porous solid. II. Higher frequency range. *The Journal of the Acoustical Society of America*, 28 (2), 179–191.
- Bohn, A., et al., 1972. Danish experiments with the French falling weight deflectometer. In: *Third international conference on the structural design of asphalt pavements, grosvenor house, Park Lane, London, England, Sept. 11–15, 1972*. vol. 1.
- Boussinesq, J., 1885. *Application des potentiels à l'étude de l'équilibre et du mouvement des solides élastiques: principalement au calcul des déformations et des pressions que produisent, dans ces solides, des efforts quelconques exercés sur une petite partie de leur surface ou de leur intérieur: mémoire suivi de notes étendues sur divers points de physique, mathématique et d'analyse*. vol. 4. Gauthier-Villars.
- Burmister, D.M., 1945a. The general theory of stresses and displacements in layered soil systems. III. *Journal of Applied Physics*, 16 (5), 296–302.
- Burmister, D.M., 1945b. The general theory of stresses and displacements in layered systems. I. *Journal of Applied Physics*, 16 (2), 89–94.
- Chatti, K., et al., 2017. *Enhanced analysis of falling weight deflectometer data for use with mechanistic-empirical flexible pavement design and analysis and recommendations for improvements to falling weight deflectometers*. Turner-Fairbank Highway Research Center.
- Chehab, G., et al., 2002. Time-temperature superposition principle for asphalt concrete with growing damage in tension state. *Journal of the Association of Asphalt Paving Technologists*, 71, 559–593.
- Chen, D.H., et al., 2000. Temperature correction on falling weight deflectometer measurements. *Transportation Research Record*, 1716 (1), 30–39.
- Chou, C.P., Lin, Y.C., and Chen, A.C., 2017. Temperature adjustment for light weight deflectometer application of evaluating asphalt pavement structural bearing capacity. *Transportation Research Record*, 2641 (1), 75–82.
- Di Benedetto, H., et al., 2004. Linear viscoelastic behaviour of bituminous materials: from binders to mixes. *Road Materials and Pavement Design*, 5 (sup1), 163–202.
- Díaz Flores, R., et al., 2023a. Multi-directional falling weight deflectometer (FWD) testing and quantification of the effective modulus of subgrade reaction for concrete roads. *International Journal of Pavement Engineering*, 24(1). <https://doi.org/10.1080/10298436.2021.2006651>.
- Díaz Flores, R., et al., 2022. Star-shaped Falling weight deflectometer (FWD) testing and quantification of the distribution of the modulus of subgrade reaction. In: *Computational modelling of concrete and concrete structures*. London: CRC Press, 284–293.
- Díaz Flores, R., et al., 2023b. T-shaped arrangement of geophones for rapid quantification of asymmetric behaviour of concrete slabs in central FWD tests. *International Journal of Pavement Engineering*, 24 (1), 2179050. <https://doi.org/10.1080/10298436.2023.2179050>
- Donev, V., et al., 2023. Instrumentation of field-testing sites for dynamic characterization of the temperature-dependent stiffness of pavements and their layers. *Structural Control and Health Monitoring*, 2023, Article ID 2857660. <https://doi.org/10.1155/2023/2857660>
- EN12697-26, 2018. *Bituminous mixtures - test methods - part 26: stiffness*. European Committee for Standardization.
- Ferry, J.D., 1980. *Viscoelastic properties of polymers*. John Wiley & Sons.
- Fu, G., et al., 2020. Determination of effective frequency range excited by falling weight deflectometer loading history for asphalt pavement. *Construction and Building Materials*, 235, 117792.

- García, J.A.R., and Castro, M., 2011. Analysis of the temperature influence on flexible pavement deflection. *Construction and Building Materials*, 25 (8), 3530–3539.
- Ghanizadeh, A.R., Heidarabadzadeh, N., and Jalali, F., 2020. Artificial neural network back-calculation of flexible pavements with sensitivity analysis using Garson's and connection weights algorithms. *Innovative Infrastructure Solutions*, 5 (2), 1–19.
- Gopalakrishnan, K., et al., 2013. Knowledge discovery and data mining in pavement inverse analysis. *Transport*, 28 (1), 1–10.
- Graziani, A., Bocci, M., and Canestrari, F., 2014. Complex Poisson's ratio of bituminous mixtures: measurement and modeling. *Materials and Structures*, 47 (7), 1131–1148.
- Gudmarsson, A., et al., 2014. Comparing linear viscoelastic properties of asphalt concrete measured by laboratory seismic and tension-compression tests. *Journal of Nondestructive Evaluation*, 33 (4), 571–582.
- Gudmarsson, A., et al., 2015. Complex modulus and complex Poisson's ratio from cyclic and dynamic modal testing of asphalt concrete. *Construction and Building Materials*, 88, 20–31.
- Hall, K.T., et al., 1997. *LTPP data analysis. phase I: validation of guidelines for k-value selection and concrete pavement performance prediction*. Federal Highway Administration, No. FHWA-RD-96-198.
- Han, C., et al., 2022. Application of a hybrid neural network structure for FWD backcalculation based on LTPP database. *International Journal of Pavement Engineering*, 23 (9), 3099–3112.
- Haskell, N.A., 1953. The dispersion of surface waves on multilayered media. *Bulletin of the Seismological Society of America*, 43 (1), 17–34.
- Hoffman, M.S., and Thompson, M., 1980. *Mechanistic interpretation of nondestructive pavement testing deflections*. University of Illinois at Urbana-Champaign, FHWA/IL/UI-190.
- Ioannides, A.M., 1990. Dimensional analysis in NDT rigid pavement evaluation. *Journal of Transportation Engineering*, 116 (1), 23–36.
- Ioannides, A., and Khazanovich, L., 1994. Backcalculation procedures for three-layered concrete pavements. In: *4th international conference, bearing capacity of roads and airfields* FHWA, U of Minnesota, Army Corps of Engineers, NRC Canada, FAA. vol. 1.
- Ioannides, A.M., and Khazanovich, L., 1998. Nonlinear temperature effects on multilayered concrete pavements. *Journal of Transportation Engineering*, 124 (2), 128–136.
- Ioannides, A., Barenberg, E., and Lary, J., 1989. Interpretation of falling weight deflectometer results using principles of dimensional analysis. In: *Proceedings, 4th international conference on concrete pavement design and rehabilitation*, Purdue University.
- Irfan-ul Hassan, M., et al., 2016. Elastic and creep properties of young cement paste, as determined from hourly repeated minute-long quasi-static tests. *Cement and Concrete Research*, 82, 36–49.
- Islam, M.R., Faisal, H.M., and Tarefder, R.A., 2015. Determining temperature and time dependent Poisson's ratio of asphalt concrete using indirect tension test. *Fuel*, 146, 119–124.
- Karte, P., et al., 2015. Unloading-based stiffness characterisation of cement pastes during the second, third and fourth day after production. *Strain*, 51 (2), 156–169.
- Kausel, E., and Roësset, J.M., 1981. Stiffness matrices for layered soils. *Bulletin of the Seismological Society of America*, 71 (6), 1743–1761.
- Khazanovich, L., Tayabji, S.D., and Darter, M.L., 2001. *Backcalculation of layer parameters for performance for LTPP test sections, volume I: slab on elastic solid and slab on dense-liquid foundation analysis of rigid pavements*. United States: Federal Highway Administration. Office of Engineering.
- Kim, Y.R., Hibbs, B.O., and Lee, Y.C., 1995. Temperature correction of deflections and backcalculated asphalt concrete moduli. *Transportation Research Record*, (1473), 55–62.
- Le, V.P., et al., 2023. Development and validation of a temperature correction model for FWD backcalculated moduli. *Australian Journal of Civil Engineering*, 21 (1), 1–9.
- Lee, H.S., and Kim, J., 2009. Determination of viscoelastic Poisson's ratio and creep compliance from the indirect tension test. *Journal of Materials in Civil Engineering*, 21 (8), 416–425.
- Levenberg, E., 2013. Inverse analysis of viscoelastic pavement properties using data from embedded instrumentation. *International Journal for Numerical and Analytical Methods in Geomechanics*, 37 (9), 1016–1033.
- Levenberg, E., and Shah, A., 2008. Interpretation of complex modulus test results for asphalt-aggregate mixes. *Journal of Testing and Evaluation*, 36 (4), 326–334.
- Li, M., and Wang, H., 2019. Development of ANN-GA program for back-calculation of pavement moduli under FWD testing with viscoelastic and nonlinear parameters. *International Journal of Pavement Engineering*, 20 (4), 490–498.
- Losberg, A., 1960. *Structurally reinforced concrete pavements*. vol. 29. Akademiforlaget Gumperts.
- Madsen, S.S., and Levenberg, E., 2018. Dynamic backcalculation with different load-time histories. *Road Materials and Pavement Design*, 19 (6), 1314–1333.
- Muslim, H.B., Haider, S.W., and Chatti, K., 2022. Influence of seasonal and diurnal FWD measurements on deflection-based parameters for rigid pavements. *International Journal of Pavement Engineering*, 23 (13), 4542–4553.
- Nguyen, Q.T., et al., 2021. Effect of time-temperature, strain level and cyclic loading on the complex poisson's ratio of asphalt mixtures. *Construction and Building Materials*, 294, 123564.
- Olard, F., and Di Benedetto, H., 2003. General '2S2P1D' model and relation between the linear viscoelastic behaviours of bituminous binders and mixes. *Road Materials and Pavement Design*, 4 (2), 185–224.
- Omine, K., et al., 1999. Prediction of strength-deformation properties of cement-stabilized soils by nondestructive testing. In: *Proceedings of the second international symposium on pre-failure deformation characteristics of geomaterials*. Rotterdam: Balkema, 323–330.
- Pan, E., 1989a. Static response of a transversely isotropic and layered half-space to general dislocation sources. *Physics of the Earth and Planetary Interiors*, 58 (2–3), 103–117.
- Pan, E., 1989b. Static response of a transversely isotropic and layered half-space to general surface loads. *Physics of the Earth and Planetary Interiors*, 54 (3–4), 353–363.
- Park, S.W., and Kim, Y.R., 1997. Temperature correction of backcalculated moduli and deflections using linear viscoelasticity and time-temperature superposition. *Transportation Research Record*, 1570 (1), 108–117.
- Park, D.Y., Buch, N., and Chatti, K., 2001. Effective layer temperature prediction model and temperature correction via falling weight deflectometer deflections. *Transportation Research Record*, 1764 (1), 97–111.
- Pichler, B., Lackner, R., and Mang, H.A., 2003. Back analysis of model parameters in geotechnical engineering by means of soft computing. *International Journal for Numerical Methods in Engineering*, 57 (14), 1943–1978.
- Planche, J., et al., 1998. Using thermal analysis methods to better understand asphalt rheology. *Thermochimica Acta*, 324 (1–2), 223–227.
- Rakesh, N., et al., 2006. Artificial neural networks—genetic algorithm based model for backcalculation of pavement layer moduli. *International Journal of Pavement Engineering*, 7 (3), 221–230.
- Roësset, J.M., and Shao, K.Y., 1985. Dynamic interpretation of dynaflect and falling weight deflectometer tests. *Transportation Research Record*, 1022, 7–16.
- Romeo, R.C., et al., 2023. A tandem trust-region optimization approach for ill-posed falling weight deflectometer backcalculation. *Computers & Structures*, 275, 106935.
- Roussel, J.M., et al., 2019. Numerical simulation of falling/heavy weight deflectometer test considering linear viscoelastic behaviour in bituminous layers and inertia effects. *Road Materials and Pavement Design*, 20 (sup1), S64–S78.
- Salour, F., and Erlingsson, S., 2013. Moisture-sensitive and stress-dependent behavior of unbound pavement materials from in situ falling weight deflectometer tests. *Transportation Research Record*, 2335 (1), 121–129.
- Schmid, S.J., et al., 2023. Significance of eigenstresses and curling stresses for total thermal stresses in a concrete slab, as a function of subgrade stiffness. *International Journal of Pavement Engineering*, 24 (2), 1–17.
- Sharma, S., and Das, A., 2008. Backcalculation of pavement layer moduli from falling weight deflectometer data using an artificial neural network. *Canadian Journal of Civil Engineering*, 35 (1), 57–66.
- Shoukry, S.N., William, G.W., and Riad, M.Y., 2005. *Evaluation of load transfer efficiency measurement*. Pennsylvania Transportation Institute, Pennsylvania State University.

- Smith, K.D., et al., 2017. *Using falling weight deflectometer data with mechanistic-empirical design and analysis*. vol. I. Federal Highway Administration, United States, FHWA-HRT-16-009.
- Sorgner, M., et al., 2023. Hindered thermal warping triggers tensile cracking in the cores of compressed columns of a fire-loaded tunnel segment structure: efficiency and accuracy of beam theory prediction, compared to FEM. *Applications in Engineering Science*, 14, 100128.
- Specht, L.P., et al., 2017. Application of the theory of viscoelasticity to evaluate the resilient modulus test in asphalt mixes. *Construction and Building Materials*, 149, 648–658.
- Strasse-Schiene-Verkehr, O.F., 2018a. *Rechnerische Dimensionierung von Asphaltstrassen [Mechanistic Asphalt Pavement Design, in German]*. Bundesministerium für Verkehr, Innovation und Technologie [Austrian Ministry of Transport, Innovation and Technology].
- Strasse-Schiene-Verkehr, O.F., 2018b. *Tragfähigkeitsmessungen mit dem Fallgewichtsdeflektometers [Bearing capacity measurements with the Falling Weight Deflectometer, in German]*. Bundesministerium für Verkehr, Innovation und Technologie [Austrian Ministry of Transport, Innovation and Technology].
- Thomson, W.T., 1950. Transmission of elastic waves through a stratified solid medium. *Journal of Applied Physics*, 21 (2), 89–93.
- Tutumluer, E., et al., 2009. *Nondestructive pavement evaluation using finite element analysis based soft computing models*. NEXTRANS Center (US).
- Ullidtz, P., and Stubstad, R.N., 1985. Analytical-empirical pavement evaluation using the falling weight deflectometer. *Transportation Research Record*, 1022, 36–44.
- Vandenbossche, J.M., 2007. Effects of slab temperature profiles on use of falling weight deflectometer data to monitor joint performance and detect voids. *Transportation Research Record*, 2005 (1), 75–85.
- Varma, S., and Emin Kutay, M., 2016. Backcalculation of viscoelastic and nonlinear flexible pavement layer properties from falling weight deflections. *International Journal of Pavement Engineering*, 17 (5), 388–402.
- Vidal, T., et al., 2015. Effect of temperature on the basic creep of high-performance concretes heated between 20 and 80 C. *Journal of Materials in Civil Engineering*, 27 (7), B4014002.
- Wang, H., et al., 2021. Prediction of airfield pavement responses from surface deflections: comparison between the traditional backcalculation approach and the ANN model. *Road Materials and Pavement Design*, 22 (9), 1930–1945.
- Westergaard, H.M., 1926. *Stresses in concrete pavements computed by theoretical analysis*. Public Roads.
- Westergaard, H., 1948. New formulas for stresses in concrete pavements of airfields. *Transactions of the American Society of Civil Engineers*, 113 (1), 425–439.
- Williams, M.L., Landel, R.F., and Ferry, J.D., 1955. The temperature dependence of relaxation mechanisms in amorphous polymers and other glass-forming liquids. *Journal of the American Chemical Society*, 77 (14), 3701–3707.
- Yusoff, N.I.M., Shaw, M.T., and Airey, G.D., 2011. Modelling the linear viscoelastic rheological properties of bituminous binders. *Construction and Building Materials*, 25 (5), 2171–2189.
- Zaoui, A., 2002. Continuum micromechanics: survey. *Journal of Engineering Mechanics*, 128 (8), 808–816.
- Zhang, M., et al., 2022. Numerical investigation of pavement responses under TSD and FWD loading. *Construction and Building Materials*, 318, 126014.
- Zheng, Y., Zhang, P., and Liu, H., 2019. Correlation between pavement temperature and deflection basin form factors of asphalt pavement. *International Journal of Pavement Engineering*, 20 (8), 874–883.

Appendices

Appendix 1. Standard deviations, coefficient of variation and ANOVA test from FWD experiments on the field-testing site

The standard deviations and coefficients of variations of the deflections measured during the five FWD tests are listed in Tables A1 and A2. An

Analysis of Variance (ANOVA) test is performed to check whether there are significant variations in the deflections measured during FWD tests performed in different seasons. The deflections presented in Table 2 are taken as an input, where every geophone position corresponds to a different group. The results of the ANOVA test, presented in Table A3, show that the null hypothesis is rejected. In other words, the variations in FWD results during different seasons are statistically significant.

Appendix 2. Dynamic Mechanical Analysis used for the stiffness characterisation of asphalt

Dynamic Mechanical Analysis (Planche *et al.* 1998, Chehab *et al.* 2002) is used for the evaluation of the test results. In the context of displacement-driven testing, sinusoidal strain histories were prescribed as a function of time t :

$$\varepsilon(t) = \varepsilon_0 \sin(\omega t), \quad (A1)$$

where $\varepsilon_0 = 50 \times 10^{-6}$ denotes the strain amplitude and $\omega = 2\pi f$ the angular frequency. The measured stress histories are approximated as sinusoidal evolutions by optimising the stress amplitude σ_0 and phase lag φ :

$$\sigma(t) = \sigma_0 \sin(\omega t + \varphi). \quad (A2)$$

Known values of the phase-lag and the stress/strain amplitudes allow for computing the storage modulus E'_a and the loss modulus E''_a as

$$\begin{aligned} E'_a &= \frac{\sigma_0}{\varepsilon_0} \cos \varphi, \\ E''_a &= \frac{\sigma_0}{\varepsilon_0} \sin \varphi, \end{aligned} \quad (A3)$$

see also Figure A1(a). Notably, E'_a is associated with the elastic response of the material, and E''_a with its viscous response. Both of them are used to quantify the complex modulus, E_a^* , which is defined as

$$E_a^* = E'_a + i E''_a, \quad (A4)$$

where i denotes the imaginary unit. The norm of E_a^* is also referred to as the ‘dynamic modulus’, see Figure A1(b).

The time-temperature superposition principle (Williams *et al.* 1955, Ferry 1980) is used for quantification of the dynamic modulus at temperatures and frequencies differing from the experimentally investigated values. The temperature- and frequency-dependent dynamic moduli, $|E_a^*|(T, \omega)$, are plotted in a double logarithmic diagram as a function of the angular frequency. All data points referring to the same testing temperature are shifted along the abscissa, such as to obtain a chain of data points which can be approximated by a master curve, see Figure 3(a). The latter is associated with a reference temperature, here: $T_0 = 20^\circ\text{C}$. Mathematically, this is expressed as

$$|E_a^*|(T, \omega) = |E_a^*|(T_0, \omega_r), \quad (A5)$$

where $\omega_r = \alpha_T \omega$ denotes the ‘reduced’ angular frequency, with α_T standing for the shift factor, which is a non-linear function of temperature, see Figure 3(b). The relation between the shift factor and the temperature is fitted using the Williams–Landel–Ferry equation (Williams *et al.* 1955):

$$\log(\alpha_T) = -\frac{C_1(T - T_0)}{C_2 + (T - T_0)}, \quad (A6)$$

where $C_1 = 26.1$ and $C_2 = 181.3^\circ\text{C}$ are optimal parameters for the here-investigated asphalt, see Figure 3(b).

In order to express the complex moduli as a continuous function of the reduced frequency, the rheological model 2S2P1D is used (Olard and Di Benedetto 2003, Di Benedetto *et al.* 2004). Introducing two springs, two parabolic dashpots, and one linear dashpot, the mathematical formulation of the model reads as

$$E_a^*(\omega_r) = E_0 + \frac{E_\infty - E_0}{1 + \delta(i\omega_r\tau_0)^{-k} + (i\omega_r\tau_0)^{-h} + (i\beta\omega_r\tau_0)^{-1}}. \quad (A7)$$

Equation (A7) contains seven fitting parameters. E_0 is the static modulus. It refers to the limit case of E_a^* when ω_r tends to zero. E_∞ is the glassy modulus. It refers to the limit case of E_a^* when ω_r tends to infinity. k

Table A1. Measurements from FWD experiments on the field-testing site, performed on five days: Standard deviations (from n_{FWD} tests) of the maximum deflections measured by geophones at radial distances r_i from the centre of the slab, ranging from 0 to 2.1 m.

Date	n_{FWD}	Standard deviations [mm] obtained at a radial distance of:							
		$r_1 = 0.0$ m	$r_2 = 0.3$ m	$r_3 = 0.6$ m	$r_4 = 0.9$ m	$r_5 = 1.2$ m	$r_6 = 1.5$ m	$r_7 = 1.8$ m	$r_8 = 2.1$ m
$t_1 = \text{Jul 21}$	15	± 0.0046	± 0.0017	± 0.0018	± 0.0014	± 0.0009	± 0.0009	± 0.0009	± 0.0009
$t_2 = \text{Sep 21}$	15	± 0.0045	± 0.0021	± 0.0013	± 0.0014	± 0.0010	± 0.0014	± 0.0015	± 0.0034
$t_3 = \text{Oct 21}$	17	± 0.0017	± 0.0017	± 0.0017	± 0.0015	± 0.0016	± 0.0032	± 0.0024	± 0.0017
$t_4 = \text{Jan 22}$	12	± 0.0010	± 0.0009	± 0.0008	± 0.0007	± 0.0010	± 0.0012	± 0.0006	± 0.0006
$t_5 = \text{Mar 22}$	12	± 0.0017	± 0.0028	± 0.0020	± 0.0012	± 0.0017	± 0.0012	± 0.0020	± 0.0013

Table A2. Measurements from FWD experiments on the field-testing site, performed on five days: Coefficients of variation (from n_{FWD} tests) of the maximum deflections measured by geophones at radial distances r_i from the centre of the slab, ranging from 0 to 2.1 m.

Date	n_{FWD}	Coefficients of variation obtained at a radial distance of:							
		$r_1 = 0.0$ m	$r_2 = 0.3$ m	$r_3 = 0.6$ m	$r_4 = 0.9$ m	$r_5 = 1.2$ m	$r_6 = 1.5$ m	$r_7 = 1.8$ m	$r_8 = 2.1$ m
$t_1 = \text{Jul 21}$	15	2.49%	0.99%	1.25%	1.13%	0.87%	1.00%	1.25%	1.48%
$t_2 = \text{Sep 21}$	15	2.53%	1.34%	0.96%	1.22%	0.99%	1.78%	2.29%	6.23%
$t_3 = \text{Oct 21}$	17	1.01%	1.11%	1.30%	1.37%	1.76%	4.30%	3.83%	3.31%
$t_4 = \text{Jan 22}$	12	0.62%	0.59%	0.62%	0.61%	1.06%	1.57%	0.94%	1.16%
$t_5 = \text{Mar 22}$	12	1.01%	1.81%	1.50%	1.07%	1.81%	1.63%	3.01%	2.58%

Table A3. p -values of ANOVA tests for the null hypothesis that the deflections of all testing dates have the same value, i.e. that there are no seasonal variations on FWD results. Each ANOVA test refers to deflections measured during the five testing dates at radial distances r_i from the centre of the slab, ranging from 0 to 2.1 m.

p -values of ANOVA test obtained for deflections at a radial distance of:							
$r_1 = 0.0$ m	$r_2 = 0.3$ m	$r_3 = 0.6$ m	$r_4 = 0.9$ m	$r_5 = 1.2$ m	$r_6 = 1.5$ m	$r_7 = 1.8$ m	$r_8 = 2.1$ m
$3.72\text{E}-25$	$2.22\text{E}-36$	$4.81\text{E}-36$	$2.26\text{E}-38$	$6.36\text{E}-34$	$4.66\text{E}-24$	$7.27\text{E}-26$	$6.53\text{E}-19$

and h are exponents with numerical values between zero and one, δ and β are constants, and τ_0 is a characteristic time referring to the reference temperature. These parameters are optimised (see Table 4) such as to reproduce the shifted data points, see the solid line in Figure 3(a).

Appendix 3. Boundary value problem of the multi-layered pavement structure subjected to FWD loading

The pavement structure is represented as a body consisting of six layers with finite thickness and infinite in-plane dimensions, see Figure 1: top-concrete, bottom-concrete, asphalt, cement-stabilised layer, unbound layer, and subgrade. A cylindrical coordinate system with base vectors \mathbf{e}_r , \mathbf{e}_ϑ , and \mathbf{e}_z is introduced. The z -axis coincides with the axis of the falling

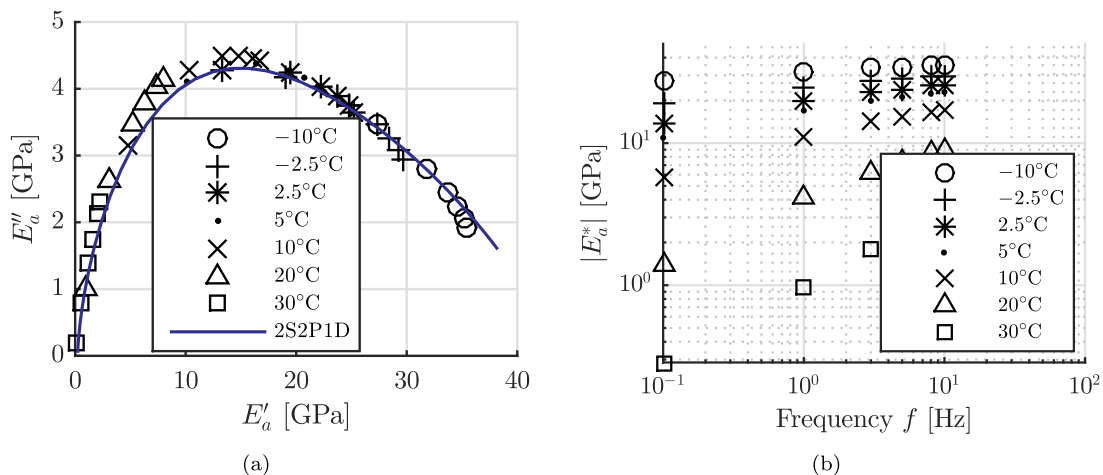
weight. It is zero at the surface of the pavement, and increases with increasing depth, see Figure 1.

The simulations represent boundary value problems of three-dimensional, static, linear elasticity. Because the problem is radial-symmetric, all quantities are constant along the circumferential coordinate ϑ . Three types of field equations are to be fulfilled at all positions \underline{x} inside the volume of the structure:

- The static equilibrium conditions read as

$$\text{div } \boldsymbol{\sigma}(r, z) = 0, \quad (\text{A8})$$

where div and $\boldsymbol{\sigma}(r, z)$ denote the divergence operator and Cauchy's stress tensor at the position (r, z) , respectively.

**Figure A1.** Results of Dynamic Mechanical Analysis: (a) loss modulus E'' over storage modulus E' ('Cole-Cole diagram'), the solid line represents the 2S2P1D model of Equation (A7), and (b) dynamic modulus, $|E^*|$, as a function of test frequency and temperature.

- The generalised Hooke's law accounting for linear elastic material behaviour in all layers reads as

$$\boldsymbol{\sigma}(r, z) = \mathbb{C}(z) : \boldsymbol{\varepsilon}(r, z), \quad (\text{A9})$$

where $\mathbb{C}(z)$ and $\boldsymbol{\varepsilon}(r, z)$ stand for the layer-specific elastic stiffness tensor and the linearised strain tensor, respectively.

- The linearised strain tensor is the symmetric part of the gradient of the displacement field

$$\boldsymbol{\varepsilon}(r, z) = \frac{1}{2} \left\{ \text{grad } \underline{u}(r, z) + [\text{grad } \underline{u}(r, z)]^T \right\}, \quad (\text{A10})$$

where grad and $\underline{u}(r, z)$ refer to the gradient operator and to the displacement vector $\underline{u} = u_r(r, z) \underline{e}_r + u_z(r, z) \underline{e}_z$, respectively.

Boundary conditions are to be fulfilled at the top and the bottom of the analysed structure:

- At the top surface of the structure, i.e. at $z=0$, pure stress boundary conditions prevail. A vertical load F is prescribed in terms of uniform normal stresses, such that the traction vector field $\underline{t}(r, z=0)$ is free of shear stresses and reads as

$$\underline{t}(r, z=0) = \begin{cases} \frac{F}{R^2 \pi} \underline{e}_z \dots r \leq R, \\ 0 \dots \dots r > R, \end{cases} \quad (\text{A11})$$

where $R=0.15$ m refers to the radius of the plate on which the load is introduced during an FWD test, and F corresponds to the force exerted by the falling weight. The assumption of uniform normal stress is deemed realistic given the high elastic modulus of the FWD loading plate, its flat surface of contact transmitting the load to the pavement, and its size (diameter = 30 cm), which is much larger than the maximum size of the aggregates (= 1.6 cm). This ensures fulfilment of the principle of separation of scales (Zaoui 2002). Notably, the size of the FWD loading plate is also much smaller than the dimensions of the slab, such that any deviations from a uniform stress state under the loading plate have a negligible effect on the structural behaviour of the slab at positions which are separated from the loading plate by a distance larger than its diameter, as stated in St. Venant's principle (Barré de Saint Venant 1855).

- At the bottom surface of the structure, i.e. at $z=h$, pure displacement boundary conditions prevail. It is prescribed that all displacements have decayed to zero, such that the displacement vector field $\underline{u}(r, z=h)$ reads as

$$\underline{u}(r, z=h) = 0. \quad (\text{A12})$$

Transition conditions are to be fulfilled at the interfaces between neighbouring layers:

- Continuity of components of the traction vectors acting on the interfaces:

$$\underline{t}(r, z=h_j^+) = \boldsymbol{\sigma}(r, z=h_j^+) \cdot \underline{e}_z = \boldsymbol{\sigma}(r, z=h_j^-) \cdot \underline{e}_z = \underline{t}(r, z=h_j^-), \quad (\text{A13})$$

where h_j refers to the z -coordinate of the bottom interface of layer j , and the subscripts + and - refer to whether this interface is approached from the layer below (+) or from the one above (-); and

- Continuity of the components of the displacement vectors (bonded interfaces):

$$\underline{u}(r, z=h_j^+) = \underline{u}(r, z=h_j^-). \quad (\text{A14})$$

The elastic stiffness tensors in Equation (A9) are, in every layer, uniform and isotropic, with layer-specific elasticity moduli E_j and Poisson's ratios ν_j

$$\mathbb{C}_j = \frac{E_j}{1-2\nu_j} \mathbb{I}_{vol} + \frac{E_j}{1+\nu_j} \mathbb{I}_{dev}, \quad (\text{A15})$$

where \mathbb{I}_{vol} and \mathbb{I}_{dev} stand for the volumetric and deviatoric parts of the symmetric fourth-order identity tensor \mathbb{I} . Their components read as $I_{ijkl} = (\delta_{ik}\delta_{jl} + \delta_{il}\delta_{jk})/2$, $I_{ijkl}^{vol} = (\delta_{ij}\delta_{kl})/3$, and $I_{ijkl}^{dev} = I_{ijkl} - I_{ijkl}^{vol}$, where δ_{ij} is the Kronecker delta, which is equal to 1 for $i=j$, and equal to 0 otherwise.

Appendix 4. Solution of a multi-layered pavement structure subjected to a vertical surface load (Pan 1989a) and rearrangement as transfer relations

In order to compute solutions for the boundary value problems defined in Equations (A8) to (A15), a system of vector functions is introduced according to Pan (1989a). Accounting for axial symmetry of the problem and for a uniform circular load acting on the top surface of the structure, it reads as:

$$\begin{aligned} \underline{L}(r, \vartheta; \lambda, m) &= S(r, \vartheta; \lambda, m) \underline{e}_z, \\ \underline{M}(r, \vartheta; \lambda, m) &= \text{grad } S = \frac{\partial S(r, \vartheta; \lambda, m)}{\partial r} \underline{e}_r + \frac{\partial S(r, \vartheta; \lambda, m)}{r \partial \vartheta} \underline{e}_\vartheta, \end{aligned} \quad (\text{A16})$$

where $S(r, \vartheta; \lambda, m)$ is a scalar function defined as

$$\begin{aligned} S(r, \vartheta; \lambda, m) &= \frac{1}{\sqrt{2} \pi} J_m(\lambda r) \exp(im \vartheta); \\ m &= 0, \pm 1, \pm 2, \dots \end{aligned} \quad (\text{A17})$$

where $J_m(\lambda r)$ denotes the Bessel function of order m , λ is a parameter variable, and i is the imaginary unit. Notably, for the axial symmetric case studied, $m=0$ and $\vartheta=0$. Equation (A17) satisfies the Helmholtz equation

$$\frac{\partial^2 S}{\partial r^2} + \frac{\partial S}{r \partial r} + \frac{\partial^2 S}{r^2 \partial \vartheta^2} + \lambda^2 S = 0. \quad (\text{A18})$$

The Ansatz functions given for the traction vector $\underline{t}(r, z)$ and displacement vector $\underline{u}(r, z)$, for the case of a load acting vertically along the z -axis read as Pan (1989a):

$$\begin{aligned} \underline{t}(r, z) &= \sigma_{rz} \underline{e}_r + \sigma_{\vartheta z} \underline{e}_\vartheta + \sigma_{zz} \underline{e}_z \\ &= \int_0^\infty T_M(z; \lambda) \frac{\partial S}{\partial r} \lambda d\lambda \underline{e}_r + \int_0^\infty T_M(z; \lambda) \frac{\partial S}{r \partial \vartheta} \lambda d\lambda \underline{e}_\vartheta + \int_0^\infty T_L(z; \lambda) S \lambda d\lambda \underline{e}_z, \\ \underline{u}(r, z) &= u_r \underline{e}_r + u_\vartheta \underline{e}_\vartheta + u_z \underline{e}_z \\ &= \int_0^\infty U_M(z; \lambda) \frac{\partial S}{\partial r} \lambda d\lambda \underline{e}_r + \int_0^\infty U_M(z; \lambda) \frac{\partial S}{r \partial \vartheta} \lambda d\lambda \underline{e}_\vartheta + \int_0^\infty U_L(z; \lambda) S \lambda d\lambda \underline{e}_z, \end{aligned} \quad (\text{A19})$$

where T_M , T_L , U_M , and U_L are the unknown traction and displacement coefficients, respectively, and $S=S(r; \lambda)$. After inserting Equation (A19) into Equations (A10), (A9) and (A8), while taking Equation (A18) into consideration, a linear system of differential equations is obtained with the unknowns T_M , T_L , U_M , and U_L , as

$$\begin{aligned} -\frac{dU_L(z)}{dz} + \frac{T_L(z)}{C_{11}} + \frac{C_{12}}{C_{11}} \lambda^2 U_M(z) &= 0, \\ -\frac{dU_M(z)}{dz} + \frac{2T_M(z)}{C_{11}-C_{12}} - U_L(z) &= 0, \\ \frac{dT_L(z)}{dz} - \lambda^2 T_M(z) &= 0, \\ \frac{dT_M(z)}{dz} + C_{12} \frac{dU_L(z)}{dz} - \lambda^2 C_{11} U_M(z) &= 0, \end{aligned} \quad (\text{A20})$$

where $C_{11} = \frac{E(1-\nu)}{(1+\nu)(1-2\nu)}$ and $C_{12} = \frac{E\nu}{(1+\nu)(1-2\nu)}$ refer to the 1111 and 1122 components of the stiffness tensor \mathbb{C} with Young's modulus E and Poisson's ratio ν . The solution of Equation (A20) may be written as a function of the initial values as

$$\underline{V}(z; \lambda) = P(z; \lambda) \cdot \underline{V}(z=0; \lambda), \quad (\text{A21})$$

where

$$\underline{V}(z; \lambda) = \begin{pmatrix} U_L(z; \lambda) \\ \lambda U_M(z; \lambda) \\ \frac{T_L(z; \lambda)}{\lambda} \\ T_M(z; \lambda) \end{pmatrix}, \quad (\text{A22})$$

and $P(z; \lambda)$ refers to the propagator matrix for one layer, defined as

$P(z; \lambda)$

$$= \begin{pmatrix} \frac{\lambda z \sinh(\lambda z)}{2(v-1)} + \cosh(\lambda z) & \frac{\lambda[(1-2\nu) \sinh(\lambda z) - \lambda z \cosh(\lambda z)]}{2(v-1)} & P_{13} & \frac{\lambda z(v+1) \sinh(\lambda z)}{2E(v-1)} \\ \frac{(1-2\nu) \sinh(\lambda z) + \lambda z \cosh(\lambda z)}{2\lambda(v-1)} & \cosh(\lambda z) - \frac{\lambda z \sinh(\lambda z)}{2(v-1)} & \frac{z(v+1) \sinh(\lambda z)}{2\lambda E(v-1)} & P_{24} \\ \frac{E\lambda[\lambda z \cosh(\lambda z) - \sinh(\lambda z)]}{2(v^2-1)} & -\frac{E\lambda^3 z \sinh(\lambda z)}{2(v^2-1)} & \frac{\lambda z \sinh(\lambda z)}{2(v-1)} + \cosh(\lambda z) & P_{34} \\ -\frac{E\lambda z \sinh(\lambda z)}{2(v^2-1)} & \frac{E\lambda[\sinh(\lambda z) + \lambda z \cosh(\lambda z)]}{2(v^2-1)} & \frac{(1-2\nu) \sinh(\lambda z) - \lambda z \cosh(\lambda z)}{2\lambda(v-1)} & \cosh(\lambda z) - \frac{\lambda z \sinh(\lambda z)}{2(v-1)} \end{pmatrix}, \quad (A23)$$

where $P_{13} = \frac{(v+1)[(4v-3) \sinh(\lambda z) + \lambda z \cosh(\lambda z)]}{2\lambda E(v-1)}$, $P_{24} = \frac{(v+1)[(3-4\nu) \sinh(\lambda z) + \lambda z \cosh(\lambda z)]}{2\lambda E(v-1)}$, and $P_{34} = \frac{\lambda[(1-2\nu) \sinh(\lambda z) + \lambda z \cosh(\lambda z)]}{2(v-1)}$. The transfer relations in the case of one layer with thickness h thus read as

$$\underline{V}(z=h; \lambda) = P(z=h, \lambda) \cdot \underline{V}(z=0; \lambda), \quad (A24)$$

where the state variables in the vectors $\underline{V}(z=h; \lambda)$ and $\underline{V}(z=0; \lambda)$ may be obtained by making use of the boundary conditions (A11) and (A12). In particular, at $z=0$, the displacement coefficients $U_L(z=0; \lambda)$ and $U_M(z=0; \lambda)$ are unknown. The traction coefficient $T_M(z=0; \lambda)$ can be determined from Equation (A11), by noting that $\vartheta_{rz} = \vartheta_{\vartheta z} = 0$, as

$$T_M(z=0; \lambda) = 0. \quad (A25)$$

Similarly, the traction coefficient $T_L(z=0; \lambda)$ can be determined by noting the mathematical property

$$\int_0^\infty J_1(R\lambda) J_0(r\lambda) d\lambda = \begin{cases} \frac{1}{R} & \dots \quad r \leq R, \\ 0 & \dots \quad r > R, \end{cases} \quad (A26)$$

and then comparing it with Equation (A19) while accounting for the boundary condition (A11), as

$$T_L(z=0; \lambda) = \frac{F}{\sigma_{zz}} \frac{R\sqrt{2\pi}}{\lambda} J_1(R\lambda), \quad (A27)$$

where F refers to the force exerted by the falling weight. At $z=h$, the traction coefficients $T_M(z=h; \lambda)$ and $T_L(z=h; \lambda)$ are unknown, while the displacement coefficients $U_M(z=h; \lambda)$ and $U_L(z=h; \lambda)$ are determined, noting Equation (A12), as

$$\begin{aligned} U_M(z=h; \lambda) &= 0, \\ U_L(z=h; \lambda) &= 0. \end{aligned} \quad (A28)$$

Inserting Equations (A25), (A27), and (A28) into (A24) enables the determination of all components of the state vectors $\underline{V}(z=0)$ and $\underline{V}(z=h)$. They can be used to solve for any particular value of z as shown in Equation (A22). The displacements, stresses and strains at that particular z may be obtained by inserting the traction and displacement coefficients obtained from (A22) into the Ansatz functions (A19), and then using the field Equations (A10) and (A9).

The solution for a multi-layered pavement follows the same steps. However, instead of Equation (A22), the transfer relations of a multi-layered pavement with n layers that have the thicknesses h_1, \dots, h_n , eval-

uated at an arbitrary position z_j within layer j , may be written as

$$\underline{V}(z; \lambda) = P(z=z_j, \lambda) \cdot P(z=h_{j-1}, \lambda) \cdots P(z=h_1, \lambda) \cdot \underline{V}(z=0; \lambda), \quad (A29)$$

where h_1, \dots, h_{j-1} refer to the z -coordinates of the bottom interfaces of layers 1 and $j-1$, respectively.

Appendix 5. Effective bending stiffness of the sandwich plate consisting of the two topmost layers of concrete

The concrete slab consists of a top concrete layer with a thickness $h_{tc} = 5$ cm and elastic modulus $E_{tc} = 34.1$ GPa, as well as a bottom layer with a thickness $h_{bc} = 22$ cm and modulus of elasticity $E_{bc} = 46.3$ GPa. Both layers have a Poisson's ratio $\nu_c = 0.2$. Accounting for bonded layers, the bending stiffness of the sandwich plate is calculated using the parallel axis theorem (Huygens-Steiner theorem), as:

$$D = \frac{E_{tc}}{1-\nu_c^2} \left(\frac{h_{tc}^3}{12} + h_{tc} d_{tc}^2 \right) + \frac{E_{bc}}{1-\nu_c^2} \left(\frac{h_{bc}^3}{12} + h_{bc} d_{bc}^2 \right), \quad (A30)$$

where d_{tc} and d_{bc} are the vertical distances between the centre of mass of the sandwich plate from the centres of mass of the top and the bottom concrete layers, respectively. Their mass densities amount to $\rho_{tc} = 2305$ kg/m³ and $\rho_{bc} = 2390$ kg/m³, respectively, see (Donev *et al.* 2023). The vertical distance of the centre of the mass of the sandwich plate from its surface, z_m , follows as

$$z_m = \frac{\rho_{tc} h_{tc} + \rho_{bc} h_{bc}}{\rho_{tc} + \rho_{bc}} = 13.65 \text{ cm}. \quad (A31)$$

Thus, $d_{tc} = 11.15$ cm, and $d_{bc} = 2.35$ cm. Inserting the given stiffness properties, thicknesses, and distances into Equation (A30) yields the effective bending stiffness of the sandwich plate consisting of the two topmost layers of concrete, as $D = 71.11$ MPa m³.

Appendix 6. Detailed results of the application of the asphalt-related temperature correction and its alternative approach

The numerical values of the application of the asphalt-related temperature correction and the alternative approach are listed in Tables A4 and A5, respectively.

Table A4. Corrected deflections: results obtained from subjecting the measured deflections of Table 2 to the asphalt-related temperature correction of Equations (5) and (6), see also Table 10.

Date	Corrected deflections [mm] at a radial distance of:							
	$r_1 = 0.0$ m	$r_2 = 0.3$ m	$r_3 = 0.6$ m	$r_4 = 0.9$ m	$r_5 = 1.2$ m	$r_6 = 1.5$ m	$r_7 = 1.8$ m	$r_8 = 2.1$ m
$t_1 = \text{Jul } 21$	0.184	0.165	0.143	0.122	0.102	0.086	0.072	0.061
$t_2 = \text{Sep } 21$	0.178	0.158	0.137	0.116	0.099	0.082	0.068	0.055
$t_3 = \text{Oct } 21$	0.177	0.157	0.135	0.113	0.094	0.077	0.063	0.053
$t_4 = \text{Jan } 22$	0.178	0.157	0.135	0.114	0.094	0.078	0.063	0.053
$t_5 = \text{Mar } 22$	0.179	0.159	0.134	0.112	0.097	0.077	0.067	0.052

Table A5. Alternatively corrected deflections: results obtained from subjecting the measured deflections of Table 2 to the correction of Equations (9) and (10).

Date	Corrected deflections [mm] at a radial distance of:							
	$r_1 = 0.0$ m	$r_2 = 0.3$ m	$r_3 = 0.6$ m	$r_4 = 0.9$ m	$r_5 = 1.2$ m	$r_6 = 1.5$ m	$r_7 = 1.8$ m	$r_8 = 2.1$ m
$t_1 =$ Jul 21	0.186	0.167	0.144	0.122	0.103	0.086	0.072	0.061
$t_2 =$ Sep 21	0.172	0.167	0.144	0.122	0.103	0.086	0.072	0.061
$t_3 =$ Oct 21	0.166	0.146	0.125	0.104	0.088	0.071	0.057	0.044
$t_4 =$ Jan 22	0.167	0.147	0.126	0.105	0.089	0.071	0.057	0.044
$t_5 =$ Mar 22	0.166	0.146	0.125	0.105	0.088	0.071	0.057	0.045